Multi-scale variations of subglacial hydro-mechanical conditions at Kongsvegen glacier, Svalbard

Coline Bouchayer[1,2], Ugo Nanni[2], Pierre-Marie Lefeuvre[3], John Hult[2], Louise Steffensen Schmidt[2], Jack Kohler[3], François Renard[1,4], and Thomas V. Schuler[2]

[1]The Njord Centre, Departments of Geosciences and Physics, University of Oslo, 0316 Oslo, Norway
[2]Department of Geosciences, University of Oslo, 0316 Oslo, Norway
[3]Norwegian Polar Institute, Tromsø, Norway
[4]ISTerre, Univ. Grenoble Alpes, Grenoble INP, Univ. Savoie Mont Blanc, CNRS, IRD, Univ. Gustave Eiffel, 38000 Grenoble, France

Correspondence: Coline Bouchayer (colili@uio.no)

Abstract. The flow of glaciers is largely controlled by changes at the ice-bed interface, where basal slip and sediment deformation drive basal glacier motion. Determining subglacial conditions and their responses to hydraulic forcing remains challenging due to the difficulty of accessing the glacier bed. Here, we monitor the interplay between surface runoff and hydro-mechanical conditions at the base of the Kongsvegen glacier in Svalbard. From spring 2021 to summer 2022, we measure both subglacial water pressure and till strength. Additionally, we derive subglacial hydraulic gradient and radius over a kilometre scale. To characterize the variations in the subglacial conditions caused by changes in surface runoff, we investigate the variations of the following hydro-mechanical properties: measured water pressure, measured sediment ploughing forces and derived hydraulic gradient and radius, over seasonal, multi-day and diurnal time-scales. We discuss our results in light of existing theories of subglacial hydrology and till mechanics to describe subglacial conditions. We find that during the short, low melt intensity season in 2021, the subglacial drainage system evolves at equilibrium with runoff, increasing its capacity as the melt season progresses. In contrast, during the long and high melt intensity season in 2022, the subglacial drainage system evolves transiently to respond to the abrupt and large water supply. We suggest that in this configuration, the drainage capacity of the preferential drainage axis is exceeded, promoting the expansion of hydraulically connected regions, and local weakening of ice-bed coupling and hence, enhanced sliding.

1 Introduction

Glacier ice loss represents one of the greatest global environmental risks in a changing climate due to its contribution to sea level rise (Moon et al., 2018; Rounce et al., 2023). Glacier flow is controlled by (i) viscous deformation of the ice, (ii) slip at the ice-bed interface, and (iii) subglacial sediment deformation. Basal motion (ii and iii) is responsible for most of the short-term velocity variations and rapid ice flow (e.g., Kamb and Engelhardt, 1991; Kamb, 2001) but underlying processes are still poorly understood due to the difficulty in observing the subglacial environment. Unravelling the response of subglacial conditions to

surface water input and its consequences for glacier dynamics is key to reduce uncertainties in future projections of ice mass loss to the oceans (e.g., Stocker, 2014; IPCC, 2019).

Rates of basal motion depend on the gravitational driving stress imposed by the glacier geometry, and on frictional properties of the glacier base which, in turn, are governed by the thermal regime and hydro-mechanical conditions (e.g., Alley, 1989; Engelhardt and Kamb, 1997). The rate of water supply from the glacier surface to the glacier base and the state of the subglacial drainage system control the basal water pressure. Basal conditions therefore vary on several time scales (e.g., hourly, daily, seasonally), inherited from typical variations of runoff, and subglacial drainage system evolution (Weertman, 1957; Lliboutry, 1968; Schoof, 2005). Following the variations of surface energy balance and rainfall, glacier surface runoff (hereafter referred to as runoff) typically displays characteristic diurnal variations, superimposed on multi-day weather cycles and a pronounced seasonality (Rothlisberger and Lang, 1987; Nienow et al., 2017). Variations in water pressure are caused both by variations in runoff as well as by the state and evolution of bulk transmissivity of the subglacial drainage system. Previous works have identified different components of the subglacial drainage system that convey and store water along the glacier bed. These include water sheets (Weertman, 1972; Walder, 1982; Creyts and Schoof, 2009), cavities in the lee of bedrock obstacles (Lliboutry, 1968; Iken, 1981), linked cavities (Kamb, 1987; Walder, 1986) and channels incised into the ice or subglacial substrate (Röthlisberger, 1972; Nye, 1976; Hooke et al., 1990; Walder and Fowler, 1994). Water sheets and cavity systems are spatially distributed across the glacier base, flow pathways are typically tortuous and these systems are characterized as hydraulically inefficient and often operate at high water pressures. In contrast, channelized drainage along preferential drainage axes is highly localized and often hydraulically efficient, which permits fast flow of water, and operates typically at low water pressures. Glaciers resting on a till base exhibit a complex subglacial drainage system. While some water drains through the pore space of the granular material, also drainage along the ice-till interface has been described and various drainage structures have been proposed. For glaciers lying on fine grain sediments, water is expected to flow through localized flow pathways termed canals. These canals are incised into the sediment and/or ice by erosion and close through the creep of ice and sediments (Walder and Fowler, 1994; Ng, 2000). Flowers and Clarke (2002a, b) proposed a macro-porous horizon as a continuum concept to comprise inter-granular pore spaces, thin films, cavities, or larger gaps.

Water pressure at the glacier base directly influences ice-bed coupling, as well as it affects shear strength of the till (Lliboutry, 1968; Clarke, 2005; Damsgaard et al., 2020; Zoet and Iverson, 2020; Hansen and Zoet, 2022; Tsai et al., 2022). This double-tracked influence gives rise to complex behavior in the relationship between water pressure and basal motion, with an exact formulation still being debated (De Fleurian et al., 2014; Benn et al., 2019; Thøgersen et al., 2019; Gimbert et al., 2021a; Gilbert et al., 2022). Whereas high water pressure weakens the ice-bed coupling and therefore promotes sliding, low water pressure has the opposite effect. Similarly, water pressure influences the yield strength of the till, for which Coulomb-plastic behavior is widely accepted. Motivation for this rheology comes from granular and soil mechanics (e.g., Schofield and Wroth, 1968; Terzaghi et al., 1996; Mitchell et al., 2005), field measurements on subglacial till deformation (Hooke et al., 1997; Kavanaugh and Clarke, 2006), laboratory experiments on till (e.g., Kamb and Engelhardt, 1991; Iverson et al., 1998; Tulaczyk et al., 2000; Iverson et al., 2007; Zoet and Iverson, 2020), inversion of subglacial mechanics from ice-surface velocities (e.g., Tulaczyk et al., 2000; Walker et al., 2012; Goldberg et al., 2014; Minchew et al., 2016; Gillet-Chaulet et al., 2016), and numerical

experiments (Iverson and Iverson, 2001; Kavanaugh and Clarke, 2006; Damsgaard et al., 2013, 2016). Pressure-gradient driven transport of water into or out of the till pore space affects rheological properties of the till and thus influence rates of sediment deformation (Iverson et al., 1995; Hooke et al., 1997; Tulaczyk et al., 2000; Hansen and Zoet, 2022; Warburton et al., 2023). Alterations in subglacial hydrological and mechanical conditions have the capacity to change the overall glacier dynamics, sometimes leading to partial or complete destabilisation (Thøgersen et al., 2019).

To investigate subglacial properties, borehole measurements have provided direct access to the glacier bed and have often been instrumented to monitor water pressure (e.g. Hubbard et al., 1995; Sugiyama et al., 2011; Andrews et al., 2014; Doyle et al., 2018; Sugiyama et al., 2019; Rada and Schoof, 2018; Rada Giacaman and Schoof, 2023). Studies based on numerous boreholes highlighted the simultaneous and different behaviour experienced by different areas of the bed (e.g., Andrews et al., 2014; Rada and Schoof, 2018). Such processes are yet poorly described by current drainage models (Flowers, 2015). For example, some areas of the glacier bed can be connected to the main subglacial drainage pathway, whereas other parts are not, and further areas even display alternating behavior (e.g., Gordon et al., 1998; Kavanaugh and Clarke, 2000). Additional studies pointed-out that some areas of the bed show signs of hydraulic isolation (e.g., Murray and Clarke, 1995; Andrews et al., 2014; Hoffman et al., 2016; Rada and Schoof, 2018). Many long-term observations have a marked spatial heterogeneity of water pressure variations, even at small spatial scales (Murray and Clarke, 1995; Iken and Truffer, 1997; Fudge et al., 2008; Andrews et al., 2014; Rada and Schoof, 2018), as well as sudden changes, indicative for reorganisation of drainage system (Gordon et al., 1998; Kavanaugh and Clarke, 2000; Schuler et al., 2002). Borehole instrumentation has been used to collect information on till shear strength using ploughmeters, on sliding rates using drag spools, and on till deformation using inclinometers (e.g., Fischer and Clarke, 1994; Fischer et al., 1998, 1999, 2001; Porter et al., 1997). Borehole studies have therefore provided crucial information on the local hydro-mechanical adaptation of the subglacial environment to changes in runoff and the following impact on glacier dynamic. Due the co-existence of different subglacial drainage system components and their temporal evolution, the interpretation of the hydro-mechanical conditions from borehole studies solely remains very local and challenging to extrapolate to the glacier-scale.

Recent studies have shown the potential of near-surface cryoseismology to bridge the gap between observations at different scales (Podolskiy and Walter, 2016), for instance to detect brittle fractures related to crevasse opening (e.g., Roux et al., 2008; Nanni et al., 2022), stick-slip motion at the glacier base (e.g., Wiens et al., 2008; Gräff et al., 2021; Köpfli et al., 2022; Hudson et al., 2023), iceberg calving (e.g., Köhler et al., 2015; Sergeant et al., 2018), or to infer subglacial hydraulic conditions across various temporal (sub-daily to multi-year) and spatial (decameter to kilometer) scales (Bartholomaus et al., 2015; Nanni et al., 2020; Lindner et al., 2020; Nanni et al., 2021; Labedz et al., 2022a). The later case is based on the principle that turbulent-water-flow generates high-frequency seismic tremor that can be used to quantify relative changes in the most active part of the subglacial drainage system (Gimbert et al., 2016; Nanni et al., 2021).

The wide range of scales over which subglacial conditions can vary and the multitude of involved processes, request appropriate sampling and analysis strategies to better understand the interplay between drainage system evolution, till rheology and consequences for basal motion. In this study, we present the results of a comprehensive, subglacial multi-sensor record, complemented by a cryoseismological dataset, all simultaneously acquired at Kongsvegen, a surge-type glacier in Svalbard.

The field instrumentation has been designed to optimize interpretation by co-locating the instruments in a single borehole and accompanying measurements of glacier surface velocity and energy-balance driven estimates of surface runoff. The records span the period from June 2021 to August 2022 and cover two contrasting melt seasons. Our results document runoff-induced variations in the subglacial hydro-mechanical conditions at different glaciologically significant time scales (diurnal, multi-day and seasonal).

2 Study area

Kongsvegen glacier (hereafter, Kongsvegen, 78° 48'N, 12° 59' E) is located near the Ny-Ålesund research station on the northwest coast of Svalbard (Fig. 1a). The glacier covers $\sim 108 km^2$, is $\sim$ 25.5 km long (in 2010, RGI, 2017) and its ice thickness at the drilling site (78° 18'N, 17° 13' E) is $\sim$ 350 m. The surface slope ranges from 0.5^o to 2.5^o with a north-western orientation (Hagen et al., 1993). The glacier drains into Kongsfjorden and its terminus is grounded below sea level. Typical for an Arctic glacier, its ice is polythermal with a temperate base and an upper layer of 50-130 m thick cold ice. Ice in the accumulation zone is temperate while it is frozen to the lateral margins in the ablation zone (Björnsson et al., 1996). The glacier rests on fine-grained sandstone and sand/silt glacio-marine sediments (Hjelle, 1993; Murray and Booth, 2010).

Kongsvegen is a surge-type glacier, with surges reported around 1800, 1869 and 1948 (Liestøl, 1988; Woodward et al., 2002). The glacier is in its quiescent phase since the last surge and exhibits low velocities of about 3 m a^{-1}. Melvold and Hagen (1998) showed that the mass transported down glacier is only about 3-20% of the annual mass gained in the accumulation area, symptomatic for a surge-type glacier in its quiescent stage. Surface velocities recorded nearby the equilibrium line indicate that the glacier is accelerating since 2014, indicating the possibility for an imminent fast flow event (Fig. 1 b).

We conducted field campaigns to install and maintain a set of instruments at Kongsvegen starting in September 2020. Borehole and surface instrumentation was completed in April 2021 and the data collected cover the period from June 26, 2021 to August 8, 2022. The following section details the instrumentation and its usage.

3 Methods

3.1 Borehole

On April 25, 2021, we drilled a borehole near the long term equilibrium line (78° 18'N, 17° 13' E, Fig. 1a) of Kongsvegen and placed instruments along the borehole and at its base. The borehole was drilled using a hot water drilling system, consisting of three high-pressure hot water machines (Kärcher HDS1000D), a 1/2 inch diameter high-pressure hose, a 2 m drill stem with a 2.3 mm diameter nozzle, a pulley, a tripod, and water tanks (three 1000-liter IBC tanks, Fig. 1d). Since the glacier was in winter conditions and liquid water was not available, water flowing out of the borehole was captured in an auxiliary hole for recycling (Fig. 1c). During drilling, the borehole water level started dropping when the drilling reached depth of 260 m, indicating a connection to an active part of the drainage system. A sediment sample collected at the bottom of the $\sim$ 350 m borehole provides evidence for the existence of a sediment layer at the glacier bed (Fig. 1e). The borehole location has been
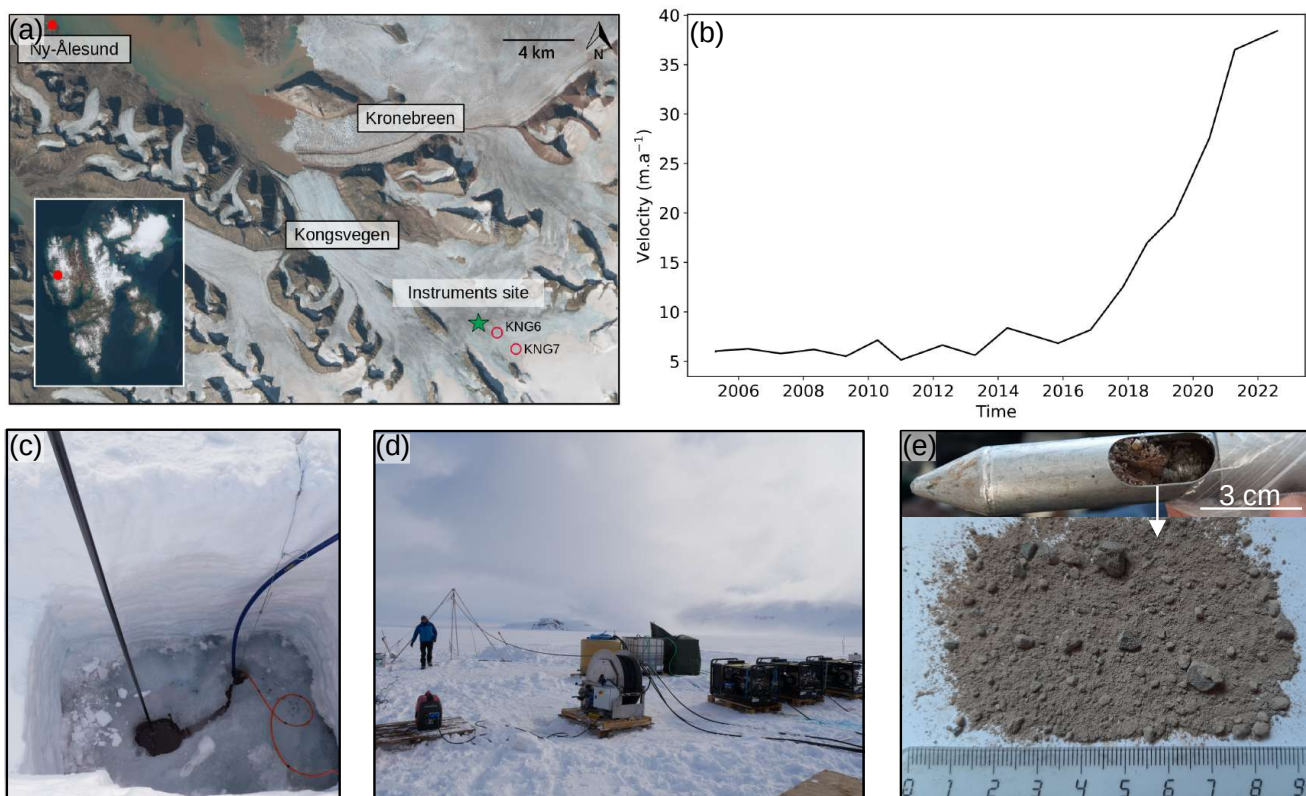
Figure 1. Study site and field methods. (a) Location of Kongsvegen in Svalbard. The green star indicates the instrument site where data were collected and the red circles indicate the position of the GNSS KNG6 and KNG7 (Credits: NPI/Copernicus Sentinel data). (b) Annual surface velocity near the equilibrium line of Kongsvegen glacier from 2005 to 2022, with an acceleration around 2014 witnessing that this glacier is closer to a surge event (personal communication from J. Kohler). (c) Main borehole with the smaller secondary borehole where the return pump is installed. (d) Drilling installation. (e) Sediment sample recovered with a sediment sampling tool at the bottom of the borehole.

chosen based on the work of Scholzen et al. (2021); Pramanik et al. (2020) who suggest the existence of a preferential drainage pathway in close proximity to this site.

At the bottom of the borehole, we installed a ploughmeter, i.e. a 1.4 m long steel rod equipped with strain gauges, to monitor
125   mechanical conditions of the subglacial till (e.g. Humphrey et al., 1993; Iverson et al., 1994; Fischer and Clarke, 1994; Porter et al., 1997; Fischer et al., 1998, 2001; Murray and Porter, 2001; Boulton et al., 2001). The tip of the instrument penetrates into the till whereas its upper part remains in the borehole and is trapped in the ice. As the glacier moves across its bed, the ploughmeter tip is dragged through the sediment, and the device bends which is sensed by the strain gauges. Strain on the ploughmeter is measured using a Wheatstone bridge for each pair of strain gauges in two perpendicular axes (Hoffmann,
130   1974). The exact insertion depth of the device into the till is unknown. However, based on previous experiences with identical devices, we estimate the penetration depth to be around 10 to 40 cm which is sufficient to ensure that all strain gauges are

immersed in subglacial material. Just above the upper end of the ploughmeter, about 1 m above the glacier bed, we installed a vibrating wire pressure sensor (Geokon 4500SH, <2 kPa accuracy and 0.5 kPa resolution) to monitor water pressure, p. Sensor readings and data recording is performed using a Campbell Scientific CR1000X data-logger, recording data at one minute intervals. Ploughmeter readings are converted to force F experienced by the instrument while being dragged through the sediment, based on a calibration performed in the laboratory prior to field deployment. To perform the calibration, loads have been applied to the horizontally fixed ploughmeter by hanging a known mass on its free end. We repeated these measurements in eight orientations (0 to 315° every 45°) using masses of 10 kg and 50 kg corresponding to loads of $\sim$100 and $\sim$500 N, respectively. After applying the calibration component-wise, we derive F from the X and Y components using Pythagoras' theorem.

3.2 Near-surface instrumentation

At $\sim$ 100m from the borehole, a three-component geophone (DiGOS, 4.5 Hz) was installed $\sim$1.5 m into the ice to ensure good coupling and prevent melt-out during summer. A DiGOS datacube, that comprises a digitizer and a data-logger, controlled the sampling rate (100 Hz) and recorded the signals. In this study, we analyse seismicity in the 3-10 Hz frequency band as a proxy for hydraulic conditions (Bartholomaus et al., 2015; Gimbert et al., 2016; Nanni et al., 2020; Lindner et al., 2020; Labedz et al., 2022a). In addition, we used data of two surface stations (KNG6 and KNG7) that recorded positions using Global Navigation Satellite System (GNSS), from which we derive surface velocities. The stations are located at distances of 740 ± 10 m (KNG6, 78.78067^oN, 13.15153^oE) and 3100 ± 10 m (KNG7, 78.76770^oN, 13.23962^oE) upstream of the drill site. Data are recorded at five-seconds intervals continuously between April 1 and September 1 when solar panels help conserving battery capacity, but only for one hour per day during the rest of the year. Gaps occurred in the time series when low battery voltage caused failure of the data logger. The GNSS data are processed assuming that the rover station is static for one hour. Then the velocities are averaged daily to reduce velocity uncertainties caused by the relatively low speed of the glacier. The Norwegian Mapping Authority's permanent network base station in Ny Ålesund is used as reference (baseline of $\sim$ 30 km). The two velocity records are merged, i.e. we consider the velocity derived from KNG6 when available and the one from KNG7 for the rest of the period (the original records for KNG6 and KNG7 can be seen in the Appendix C). We apply a one-week moving median for KNG7 velocity to smooth the record especially during the winter period when the velocities are low.

3.3 Surface runoff and meteorological conditions

The surface runoff is modelled using the CryoGrid community model (Westermann et al., 2023), coupling surface energy balance to a multi-layer snow pack model enabling simulation of glacier mass balance and freshwater runoff (Schmidt et al., 2023). The model is forced by 3-hourly fields of near surface conditions from the Copernicus Arctic Regional Reanalysis (CARRA, Schyberg et al., 2020; Yang et al., 2021) for 2021 and single-member forecasts by AROME-Arctic (Müller et al., 2017) for 2022. Meteorological forcing includes 2 m air temperature and precipitation among other variables. Differences in model results due to different forcing datasets are small in our study area (i.e., $< 2\%$ of the total runoff, Schmidt et al., 2023). The CryoGrid community model then calculates the surface energy balance to simulate the mass balance components as well

as the build-up and decay of seasonal snow. The available surface water in a grid cell is either retained in snow or firn, or runs off under the influence of gravity. The retention is governed by the hydraulic conductivity of the snow, parameterized based on snow grain size, density, and effective water saturation. Depending on temperature conditions, retained water may refreeze, thereby releasing latent energy. Once the retention capacity of a layer is reached, excess water may run off with a time scale depending on surface slope. Schmidt et al. (2023) estimated a standard error of runoff of 0.12 m w.e.a^{-1}. The surface runoff is modelled on a 2.5 by 2.5 km grid and we assume that all runoff produced within an area of 6.25 km^2 upstream of our borehole is conveyed at the base without any delay. Since our analysis considers relative changes, only the timing but not the absolute magnitude are of interest. We calculate the surface runoff transiting through our study area by integrating all runoff produced in its upglacier hydrological basin, the latter computed using the TopoToolbox (Schwanghart and Scherler, 2014). The temporal resolution of the runoff output is three hours. A complete description of the workflow is given by Schmidt et al. (2023). Using simulated surface runoff to represent local discharge through a given cross-section implicitly assumes transfer of water between the surface and the base within short time, which is supported by in-situ observations from other Svalbard glaciers similar to Kongsvegen (Benn et al., 2009; Gulley, 2009; Bælum and Benn, 2011; Irvine-Fynn et al., 2011) and the good agreement between daily values of simulated runoff and measured proglacial discharge at the catchment scale (Schmidt et al., 2023). Therefore, we consider relative variations in surface runoff to represent those of subglacial discharge, even though large uncertainties on the magnitude of the subglacial discharge remain.

3.4 Derived subglacial variables

3.4.1 Seismic power, hydraulic radius and hydraulic gradient

We calculate the seismic power from the vertical component of the ground velocity using Welch's method over a two-second time window with a 50% overlap (Welch, 1967; Beyreuther et al., 2010) within the frequency band 3 to 7 Hz. Our choice of this frequency band is based on the dominance of turbulent-water flow-induced seismicity in this band (Bartholomaus et al., 2015; Gimbert et al., 2016; Nanni et al., 2020, 2022), as opposed to bedload transport that generates seismicity at higher frequencies (Gimbert et al., 2016). This has been previously observed in other glacial settings (e.g., Preiswerk and Walter, 2018; Lindner et al., 2020; Labedz et al., 2022b; Clyne et al., 2023). Variations in this frequency band are related to changes in hydraulic radius, R, i.e. the ratio of the cross-sectional area of a channelized flow to its wetted perimeter, and in hydraulic gradient, S, i.e. the water pressure gradient in the along flow direction. For open flow, R scales with flow depth and S with slope in the along flow direction. For glaciers, Gimbert et al. (2016) expressed P as a function of R and S. The relative changes of these variables are derived from relative changes in P and Q (Gimbert et al., 2016):

$$\frac{S}{S_{ref}} = \left(\frac{P}{P_{ref}}\right)^{24/41} \left(\frac{Q}{Q_{ref}}\right)^{-30/41} \tag{1}$$

$$\frac{R}{R_{ref}} = \left(\frac{P}{P_{ref}}\right)^{-9/82} \left(\frac{Q}{Q_{ref}}\right)^{-21/41} \tag{2}$$

where the subscript ref represents a reference state that must be defined over the same period for Q and P, but not necessarily for R and S. In our case, the reference state was taken on June 24, 2021 ($Q_{ref} = 0.08$ m^3 s^{-1} and $P_{ref} = 180.59$ dB) which corresponds to the pre-melt season 2021 value against which we want to evaluate relative changes happening during the melt season. The method is described in detail by Gimbert et al. (2016). Here, we neglect changes in conduit shape, fullness and number as they have limited impact on the derivation of R and S (Gimbert et al., 2016; Nanni et al., 2020). This approach allows to estimate the evolution of R and S of the dominating drainage system over an area of c. 1 km^2 around the seismic station (Gimbert et al., 2016; Nanni et al., 2020; Lindner et al., 2020; Nanni et al., 2021; Labedz et al., 2022a). To simplify notation, we hereafter refer to R/R_{ref} and S/S_{ref} as R and S respectively.

We evaluate our results against theoretical considerations relating P and Q (Gimbert et al., 2016), and hydraulic properties and Q (Röthlisberger, 1972; Nanni et al., 2020) to discuss the state of the subglacial drainage system during the period of our records. The scaling relationship proposed by Gimbert et al. (2016) defines cases where steady-state channels incised in the ice adapt to changes in Q by only adjusting R (constant S) or the opposite case (constant R). Nanni et al. (2020) adapted Röthlisberger's (1972) theory to derive scaling relationships between R and Q, and S and Q, both for a steady-state channel evolution incised in the ice as well as for a channel of static cross-sectional area evolving thus as a rigid pipe (Table 1).

Table 1. Scaling relationships between P and Q, S and Q, and R and Q for special cases, derived by Gimbert et al. (2016) and Nanni et al. (2020) from Röthlisberger (1972) theory to assess variations in channelized drainage conditions.

Context	Relation	Reference
Change in runoff occurring at constant hydraulic radius	$P \propto Q^{14/3}$	Gimbert et al. (2016)
Change in runoff occurring at constant hydraulic gradient	$P \propto Q^{5/4}$	
Steady-state channel	$R \propto Q^{9/22}$	Röthlisberger (1972); Nanni et al. (2020)
	$S \propto Q^{-2/11}$	

3.5 Processing of time series, catalog of events and classification

To characterize the responses of the subglacial environment to runoff, Q, we analyse the responses of the subglacial variables recorded in the present study, i.e. the force, F, the water pressure, p, and derived, i.e., the turbulent-water-flow-induced seismic power, P, the hydraulic radius, R and the hydraulic gradient, S, in terms of phase relationship to Q. Here we use the term phase to characterize the time relationships between one of the subglacial variables and events detected in the time series of Q. These phase relationships are analysed at three different, glaciologically relevant time scales: seasonal, multi-day, and diurnal. To extract the corresponding components at these three time scales, we filtered the time series using a low-pass filter with cutoff at 20 days, a band-pass filter between four and eight days, and a band-pass filter between six hours and 36 hours, respectively. We subdivide the multi-day and diurnal time series into individual events based on Q variations. We define an event by two subsequent minima of Q within the bandwidth investigated. We normalize both Q and the subglacial variables by their respective maxima and subdivide the time into 50 equidistant steps. We choose the number of time steps was chosen empirically as the minimum number of data points that preserves the shape and characteristics of the event time series (see also

Appendix B, Fig. B1). We synthesize the different responses of each subglacial variables to changes in Q using a classification scheme (Fig. 2). Our workflow resembles that developed by Nanni et al. (2020) to understand sub-glacial hydrology on hard-bed glaciers, and by Javed et al. (2021) to study storm-induced hydrological conditions variations. The period of records is subdivided; at a multi-day time scales into twelve events (melt season 2021, see Appendix D, Tab. D1) and eight events (melt season 2022, see Appendix D, Tab. D2); and at a diurnal time scale into 96 events (melt season 2021, see Appendix D, Tab. D3) and 85 events (melt season 2022, see Appendix D, Tab. D4).
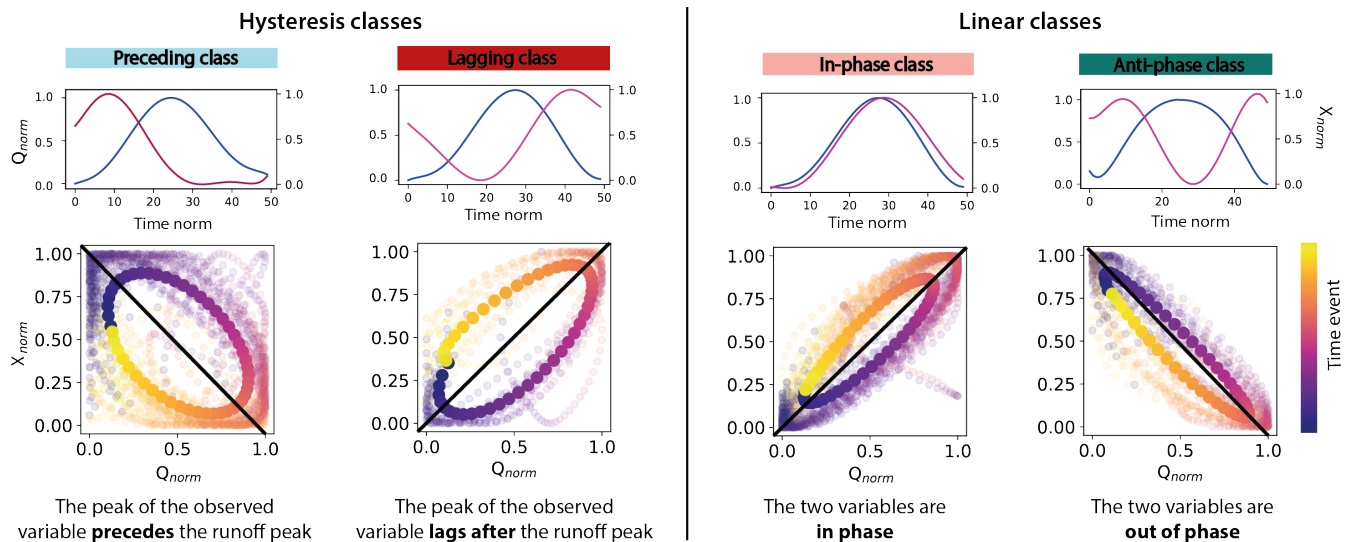
Figure 2. Phase relationship classification for events. Below each class, the plots in the first row correspond to a representative event for this class with runoff (Q_{norm}) plotted in blue and one subglacial variable (X_{norm}, with X being F, P, p, R or S) plotted in pink against time. The magnitude of the variables is normalised between 0 and 1 and the time is re-sampled into 50 time steps. The plots in the second row show the shape of the relationship between the two variables after classification. The solid color points refer to the mean behavior in this class, all individual events from the filtered time series are shown in shaded colors. The black line is the linear regression fitted to the scatter plot. *Preceding class* and *Lagging class* correspond to clockwise or anti-clockwise hysteresis (or time-lag) between the runoff, Q, and the observed variable, while *In-phase class* and *Anti-phase class* correspond to linear relationships. The color scale indicates chronology.

Our classification scheme is based upon the following metrics: the slope m of the linear regression between the subglacial variable X (with X being F, P, p, R or S) and Q (black line, Fig. 2); the squared residuals, RSS, between the linear regression and the $X_{norm} - Q_{norm}$ hysteresis loop; θ whose sign indicates the direction of the hysteresis loop. The spread of the data relative to the regression is quantified by (Appendix F, Fig. F1b):

$$RSS = \sum_{i=1}^{n} r_i^2 \tag{3}$$

where r_i are the residuals of the regression.

The parameter θ expresses the asymmetry of the response with respect to the forcing and its sign determines whether the hysteresis is clockwise or counterclockwise. We compute θ by comparing the mean of the subglacial variable considered during the rising limb of Q, $\overline{X}_{Q_{rising}}$, to its counterpart during decreasing Q, $\overline{X}_{Q_{falling}}$ (Appendix F, Fig. F1a):

$$\theta = \frac{\overline{X}_{Q_{rising}} - \overline{X}_{Q_{falling}}}{\overline{X}_{Q_{falling}}} \tag{4}$$

The sign of θ indicates whether the signal precedes ($\theta > 0$) or lags ($\theta < 0$) Q. Events are classified according to the phase relationship between Q and the subglacial variable. We distinguish four classes, representing the following cases (Fig. 2):

- *Preceding class*: The subglacial variable considered precedes Q, $RSS > 2$ & $\theta>0$,

- *In-phase class*: The subglacial variable considered lags behind Q, $RSS > 2$ & $\theta<0$,

- *In-phase class*: The subglacial variable considered and Q vary in phase, $RSS \leq 2$ & $m>0$,

- *Anti-phase class*: The subglacial variable considered and Q vary in anti-phase, $RSS \leq 2$ & $m<0$.

To discriminate between linear and hysteresis relations, we use a threshold of $RSS = 2$, corresponding to a phase difference of about $\pi/10$ for two sinusoidal variations. Our analysis does not target a two member classification (steady-state or not), but a four member classification of phase relationships which are subsequently interpreted.

4 Results

4.1 Overview over the dataset

The meteorological conditions extracted from CARRA/AROME-Arctic, the velocity, u_s, the runoff, Q, the turbulent-water-flow-induced seismic power, P, the water pressure, p and the force acting on the ploughmeter, F, are displayed in Figure 3. We obtain time series covering two melt seasons (2021 and 2022, Fig. 3) and one winter period (Appendix A, Fig. A1). The meteorological conditions (Figure 3a and b) control timing and volume of Q resulting from meltwater production or rainfall (Figure 3c and d). We note that the dataset covers two very different melt seasons. While the 2021 melt season is short (67 days from July 1, 2021 to September 6, 2021), marked by low temperature oscillating around 0^oC and continuous low runoff (lower than 20 m^3 s^{-1}), the 2022 melt season is long (at least 83 days because we do not capture the end of this melt season, from May 25, 2022 to August 16, 2022) marked by high temperatures (up to 7^oC) and frequent and large excursions of runoff above 20 m^3 s^{-1}.

In response to temperature and rainfall variations, Q displays variations on several time scales (Fig. 3c and d, blue line): (i) the seasonal time scale (>20 days) is marked by Q generally being limited to the melt season; (ii) the multi-day superimposed time scale (four to eight days), typically reflects weather variability (warm-spells, e.g., Fig. 3c②, or rainfall, e.g, Fig. 3c④); (iii) and being melt-dominated, the pronounced diurnal variability of Q reflects the diurnal variability of surface energy balance.
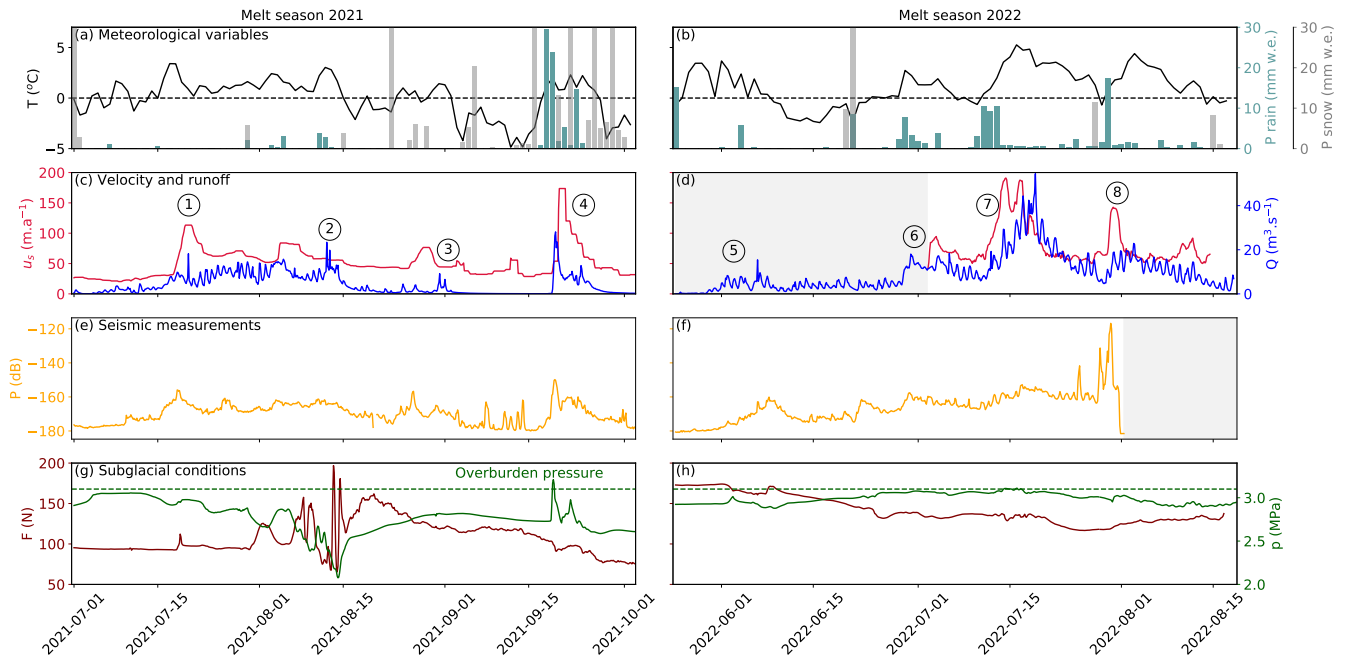
Figure 3. Time series of physical quantities measured during the melt seasons 2021 (a, c, e, g) and 2022 (b, d, f, h).: (a-b) Temperature (black line), snow fall (grey bars) and rainfall (light blue) from CARRA/AROME-Artic (Schmidt et al., 2023). The three variables are extracted for the grid point closest to the borehole location. (c-d) Modelled runoff (blue) and measured glacier surface velocity (red). Circled numbers refer to episodes described in the main text. (e-f) seismic power recorded at the surface of the glacier in the 3-10 Hz frequency band (yellow). (g-h) Borehole water pressure (green) and force acting on the ploughmeter (dark red). Blue shaded areas represent the melt seasons. Grey shaded areas represent periods of missing data. The complete uninterrupted record spanning from spring 2021 to the end of summer 2022 is presented in Appendix A, Fig. A1.

The turbulent-water-flow-induced seismic power P (Fig. 3e and f, yellow) follows the variations in Q throughout the recorded period, increasing at the beginning of the two melt seasons and decreasing towards their end. Such behaviour has been previously observed in other settings and confirms the sensitivity of the selected frequency band to Q (Bartholomaus
265 et al., 2015; Gimbert et al., 2016; Nanni et al., 2020, 2021; Lindner et al., 2020; Labedz et al., 2022a). In contrast, variations in water pressure in the borehole p do not follow Q variations in a simple way (Fig. 3g and h, green). At the beginning of the 2021 melt season, p is high, close to the overburden pressure. As Q continues to increase, p decreases until it reaches its minimum values ($\sim$2 MPa) after peak Q marked by ②. p increases again during the winter to reach a value (2.9 MPa) close to overburden pressure (3.2 MPa, (Appendix A, Fig. A1d). In the second year of the record, p remains high and increases to
270 the overburden pressure in mid-July 2022 before decreasing again to levels close to its winter value (2.9 MPa) at the end of August.

Similar to p, the force acting on the ploughmeter, F, shows different behaviors between the two melt seasons (Fig. 3g and h, dark red). During the melt season 2021, it remains fairly stable until August 2021, when it suddenly undergoes large amplitude

($\sim$150 N maximum amplitude), high-frequency variations. As the instrument site becomes snow-free around August 15, 2021 (Fig. 3a), F gradually decreases towards the end of the melt season until it reaches its minimum value in early October 2021 ($\sim$ 70 N). At the end of September occurs a major precipitation episode (Fig. 3c④), with heavy rainfall going over to snowfall as the temperature dropped. F does not react to this event. After this precipitation event, F gradually increases until it stabilizes at $\sim$ 170 N in January 2022. Note that this value is almost twice the value observed before the melt season 2021 ($\sim$ 90 N).

The surface velocity of the glacier is related to Q-induced changes and several glacier speed-up episodes are identified early in the melt season 2021, when Q increased (Fig. 3c①), during large rainfall episode (Fig. 3c④), and during sudden influx of meltwater during the 2022 melt season (Fig. 3d, ⑥, ⑦, ⑧).

To interpret the responses of the subglacial drainage system and glacier dynamics to variations in runoff, Q, we analyze the data using a phase relationship analysis on seasonal (above 20 days, Sec. 4.2), multi-day (four to eight days, Sec. 4.3), and diurnal (six hours to 36 hours, Sec. 4.4) time scales.

4.2 Analysis of seasonal variations

To examine the phase relationship between the subglacial variables and Q at the seasonal scale, all time series are low-pass filtered with a cut-off frequency of 20 days. We first describe the results obtained for the melt season 2021 and then for the melt season 2022.

We divided the melt season 2021 into four regimes. At the beginning of the melt season, the preferential drainage axis evolves predominantly by adjusting its capacity R (constant S, Fig. 4a, 1). As Q increases, this is followed by an adjustment of S at constant R (Fig. 4a, 2). When Q decreases in August 2021, the preferential drainage axis evolves by adjusting R (constant S; Fig. 4a, 3). At the end of the melt season 2021, the trajectory of P is indicative of an adjustment of S (Fig. 4a, 4). The $R - Q$ trajectory is parallel to the scaling relationships for channels evolving at steady-state (Fig. 4b) and we observe that the $S - Q$ trajectory follows the steady-state relationship, though not always strictly parallel (Fig. 4c). We observe that the $p - Q$ relationship is characterised by a clockwise hysteresis (Fig. 4d) indicating that the peak in p precedes the peak in Q. The linear relationship between F and p during the first half of the melt season indicates that the two subglacial variables are anti-correlated (Fig. 4e) and, at the end of the melt season, $F - p$ trajectory shows a counter-clockwise hysteresis, indicating the the peak in F lags after the peak in p (Fig. 4e).

Similar as in 2021, the melt season 2022 can be divided into four regimes, but these phases describe different behaviours. At the beginning of the melt season, the preferential drainage axis evolves predominantly by adjusting R (Fig. 4f, 1), as observed in 2021. Then, the preferential drainage axis briefly leaves this regime to follow an evolution that is not described by the theoretical relations and that are neither governed by constant R nor constant S (Fig. 4f, 2). This is followed by a return to a regime indicative of predominant adjustment of S (constant R) for the remaining increase in runoff (Fig. 4f, 3). The runoff decrease phase is not completely captured in the record because the records do not extend to the end of the melt season 2022. However, for the period covered by data, we observe that the evolution of P is not indicative for neither constant R nor constant S (Fig. 4f, 4). We identify these four phases in the relationship of S and Q. During phases 1 and 3, the behavior is indicative of a preferential drainage axis evolving in equilibrium with Q (Fig. 4g and h, 1 and 3) and during phases 2 and 4, the observed
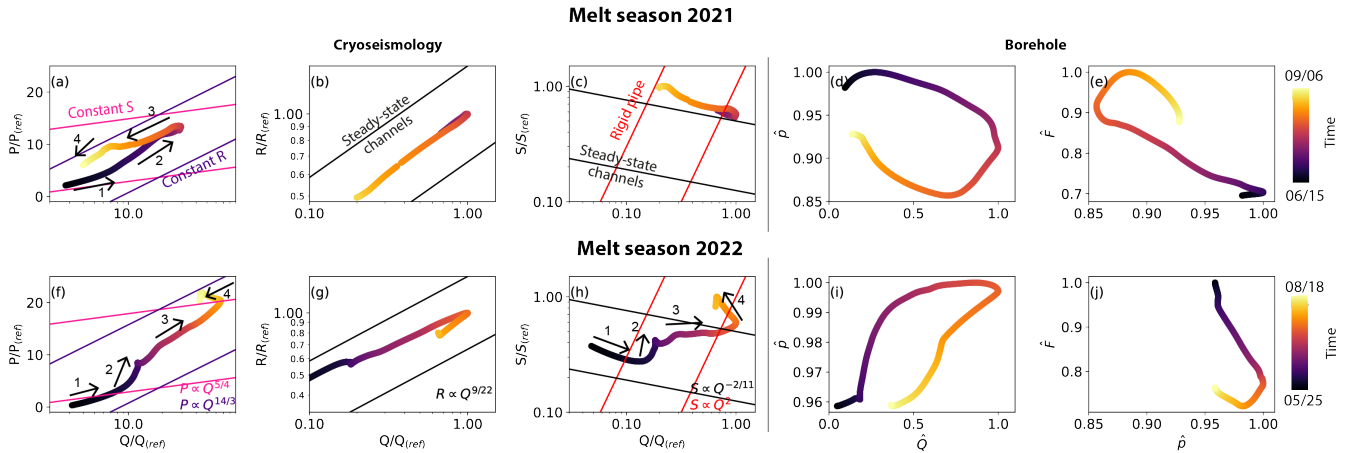
Figure 4. Relationships between two variables at the seasonal scale for the melt seasons 2021 and 2022. Color scales are scale to the number of days in each melt seasons. Note that the variables R and S have been derived only from July 19 to August 31, 2021 and from May 25 to August 1, 2022 explaining that the color scale is not entirely represented (outside of these periods, runoff is too low to derive R and S, see Section 3.4.1. P, R and S are expressed in terms of relative changes to a reference stage, in our case on June 14, 2021, when $Q_{ref} = 0.2 \text{m}^3$ s^{-1}. (a) and (f) Relationships between scaled runoff (Q/Q_{ref}) and scaled turbulent-water-flow-induced seismic power (P/P_{ref}). The x-axis is in logarithmic scale. The superimposed lines show the relations derived by Gimbert et al. (2016) for a constant hydraulic gradient (pink lines, $P \propto Q^{5/4}$) and for a constant hydraulic radius (purple curve, $P \propto Q^{14/3}$). (b) and (g) Relationship between scaled runoff (Q/Q_{ref}) and scaled hydraulic radius (R/R_{ref}). Both x and y-axes are in logarithmic scale. Superimposed lines show the relations of steady-state preferential drainage axis evolution (Nanni et al. (2020), $R \propto Q^{9/22}$). (c) and (h) Relationship between scaled runoff (Q/Q_{ref}) and scaled hydraulic gradient (S/S_{ref}). Both x and y-axes are in logarithmic scale. Superimposed lines show the relations of Nanni et al. (2020) for a preferential drainage axis at steady-state (black lines; $S \propto Q^{-2/11}$) and for a preferential drainage axis evolving as a fixed cross sectional area channel referred to as rigid pipe (red line; $S \propto Q^2$). For the panels a to c and f to h, we interpret our observations as aligning with one of the scenarios detailed in Gimbert et al. (2016); Nanni et al. (2020), where the slope of the hysteresis curve is parallel to the theoretical scaling. (d) and (i) Relationship between normalised water pressure and normalised runoff. (e) and (j) Relation between normalised force and normalised water pressure. Arrows indicate the direction of time and numbers refer to different periods described in the main text. The numbers do not correspond to the same periods between each panels and are unrelated to the periods identified by the circled numbers in Figure 3.

behavior more closely resembles that of a rigid-pipe (Fig. 4g and h, 2 and 4). As opposed to the melt season 2021, p and Q evolve almost in parallel. At the beginning of the melt season, p and Q are positively related even though the relationship displays some clockwise hysteresis (Fig. 4i). As for the melt season 2021, F and p are anti-correlated (Fig. 4j).

4.3 Analysis at multi-day scale

To understand the relationships on time-scales of weather variations, we filtered the time series with a band-pass filter, removing the variations with periods below four days and above eight days. Then, we applied our phase relationship classification scheme
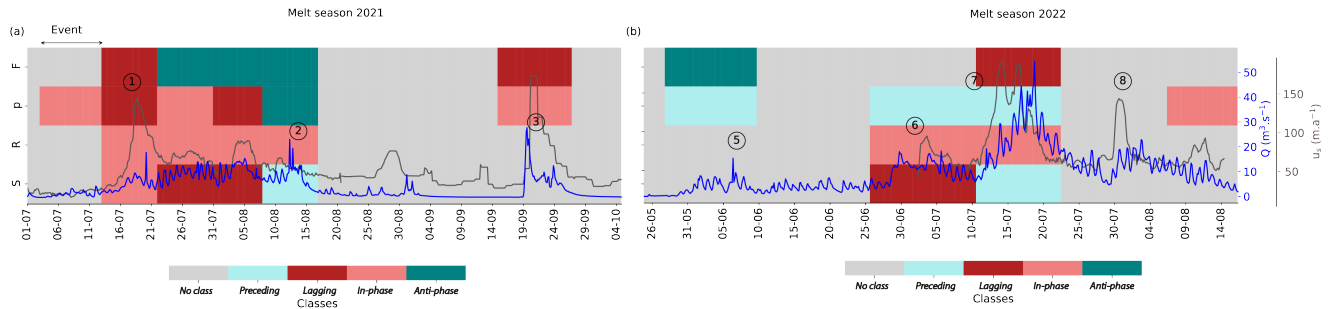
Figure 5. Phase relationships between the subglacial variables (S, R, p and F) and runoff (Q) at a multi-day time scale. (a) shows the classification for the melt season 2021, and (b) for the melt season 2022. Grey fields refer to periods when data is missing and the vertical grey lines delineate the events. *Preceding class* and *Lagging class* correspond to clockwise or anti-clockwise hysteresis between the runoff and the observed variable while classes *In-phase class* and *Anti-phase class* correspond to linear relationships. In addition, the time series of velocity (grey line) and runoff (blue line) are super-imposed on each panel. Circled numbers refers to episodes described in Section 4.1.

to each event (Fig. 5). We investigate the phase relationships between the subglacial variables (the force, F, the water pressure,
315   p, the hydraulic radius, R, the hydraulic gradient, S) and the runoff, Q, for each event during the melt seasons in 2021 (eleven events) and 2022 (eight events, see Section 3.5). Similar phase relationships are observed during both melt seasons between (i) R and Q and (ii) S and Q. During both melt seasons, R evolves in phase with Q (*In-phase class*, Fig. 5 a and c) and S at the beginning of the melt season 2021 (*In-phase class*, Fig. 5a). We cannot compare the relationship between S and Q at the beginning of the melt season 2022 as we have removed the events due to the inconsistency between the filtered data and the
320   raw data during this period (Appendix G, Fig. G1). For the remaining part of the season, the behaviour of S in response to Q is very similar in 2021 and 2022. During the first half of both melt seasons, S is first lagging after Q (*Lagging class*, Fig. 5a and c). During Q important excursions occurring in August 2021 (Fig. 5b②) and July 2022 (Fig. 5d, ⑦), S precedes Q changes (*Preceding class*, Fig. 5a and b). In contrast to the phase relationships of R and S to Q, F do not show the same time-evolution across both melt seasons but $F - Q$ phase relationship is sensitive to glacier acceleration. During high velocity episodes (Fig.
325   5b and d, ①, ③, ⑦), F systematically lags behind Q (*Lagging class*, Fig. 5a and c). Conversely, when velocity is low and stable during the melt season 2021 (Fig. 5b and d, from ① to ③), F is anti-correlated with Q (Fig. 5a and c). We do not have GNSS data in 2022 at this period to compare with the observations in 2021. $p - Q$ phase relationship is contrasted between the melt season 2021 and 2022. On one hand, $p - Q$ phase relationship cannot be easily linked to specific Q regimes or speed-up episodes and shows various responses across the melt season 2021 (*Lagging class*, *In-phase class* and *Anti-phase class*, Fig.
330   5a and c). On the other hand, p always precedes Q during the melt season 2022 (*Preceding class*, Fig. 5c).

Figure 6 shows the comparison between the multi-day scale observations of P, R and S and the scaling relationships by Gimbert et al. (2016) and Nanni et al. (2020). At the beginning of the melt season 2021 (July 2021), the slope of the $P - Q$ relation exceeds those of the relations expected for a constant R or constant S before aligning with a slope indicative of a preferential drainage axis evolving its capacity at a constant S in the middle of the melt season (August 2021, Fig. 6a). At the
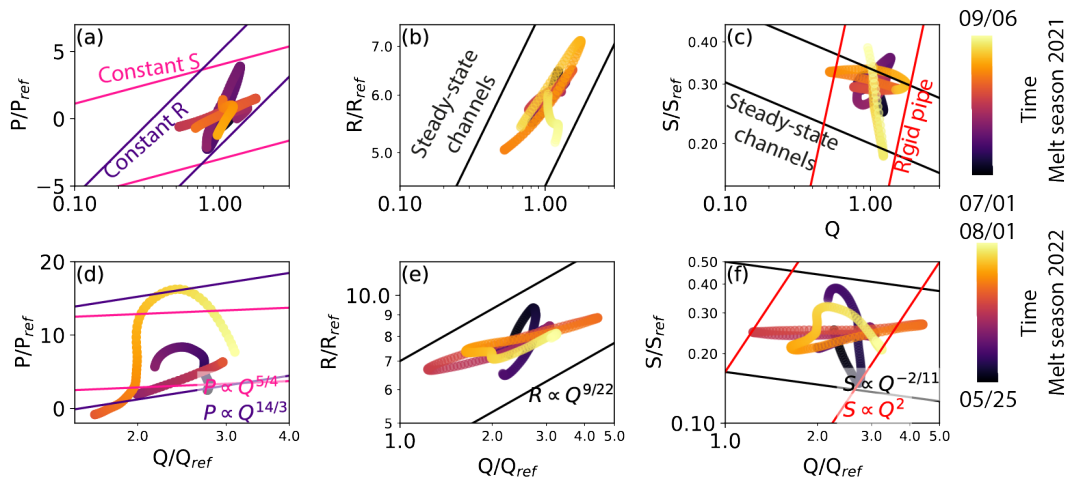
Figure 6. Relationship between the subglacial variables (P/P_{ref}, R/R_{ref}, S/S_{ref}) and runoff (Q/Q_{ref}) during the two melt seasons at a multi-day time scale. The color scale indicates the timing during both melt seasons and is scaled according to the length of each season. (a) and (d) Relationship between scaled runoff (Q/Q_{ref}) and scaled turbulent-water-flow-induced seismic power (P/P_{ref}). The x-axis is in logarithmic scale. The superimposed lines show the relations derived by Gimbert et al. (2016) for a constant hydraulic gradient (pink lines, $P \propto Q^{5/4}$) and for a constant hydraulic radius (purple curve, $P \propto Q^{14/3}$). (b) and (e) Relationship between scaled runoff (Q/Q_{ref}) and scaled hydraulic radius (R/R_{ref}). Both, x and y-axis are in logarithmic scale. Superimposed lines show the relations for a steady-state channel evolution (Nanni et al. (2020) $R \propto Q^{9/22}$). (c) and (f) Relationship between scaled runoff (Q/Q_{ref}) and scaled hydraulic gradient (S/S_{ref}). x and y axes are in logarithmic scale. Superimposed lines show the relations of Nanni et al. (2020) for a channel evolution (black lines; $S \propto Q^{-2/11}$) and for a channel evolving as a rigid-pipe of static cross-section (red line; $S \propto Q^2$).

end of the melt season, P switches back to the behavior seen at the beginning of the melt season 2021 (Fig. 6a). In general, R evolves with Q similar to what is expected for a steady-state channel (Fig. 6b) whereas S shows a more complex behaviour that is difficult to disentangle (Fig. 6c).

During the melt season 2022, the evolution of P is neither clearly dominated by a constant R or S (Fig. 6d). In general, R increases with Q but at a slope that differs from the one expected for steady-state channels (Fig. 6e). As in 2021, the evolution of S exhibits complex behaviour at this scale during the melt season 2022 (Fig. 6f).

4.4 Analysis of diurnal variations

Symptomatic for meltwater runoff, Q exhibits strong diurnal variations. To examine the glacier response to changes in Q at a diurnal scale, we filtered the time series using a band pass filter, cutting off variations beyond the lower and upper limits of six hours and 36 hours, respectively (Fig. 7) respectively to capture the primary diurnal frequency (around 24 hours) and also to account for some variations and fluctuations around this period. The filtered time series are then subdivided into 95 events in 2021 and 84 events in 2022 (see Section 3.5) and we applied our phase relationship classification scheme.
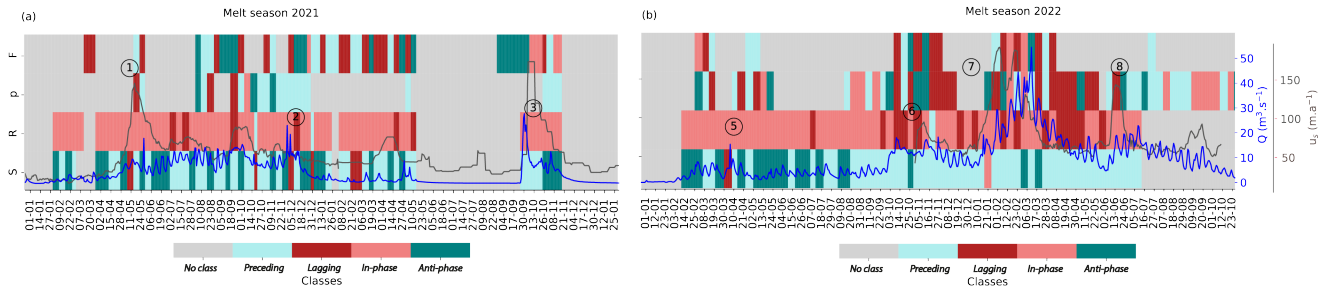
Figure 7. Phase relationships between the subglacial variables (S, R, p and F) and runoff (Q) at a diurnal time scale. (a) Classes from the phase relationship classification per event for the melt season 2021 and (b) for the melt season 2022. Grey fields refer to periods when data is missing and the vertical grey line delineate the events. In addition, the time series of velocity (grey) and runoff (blue) are super-imposed on each panel. Circled numbers refer to episodes described in Section 4.1.

The phase relationships between the subglacial variables (the force, F, the water pressure, p, the hydraulic radius, R, the hydraulic gradient, S) and Q on a diurnal time scale are displayed in Figure 7. Results indicate that R and S show consistent phase relationships with Q during both melt seasons, alternating between *Lagging class* and *Preceding class*, and *Preceding*

350 *class* and *Anti-phase class*, respectively (Fig. 2). However, $p - Q$ and $F - Q$ phase relationships vary across all classes without an easily identifiable pattern (Fig. 7a-c). Except for during short episodes, p and F do not display pronounced diurnal variations (Appendix H, Fig. H1). Therefore, we focus on the analysis of diurnal variations on the responses of P, R and S.

During the 2021 melt season, we observe that R mostly varies in phase with Q (*In-phase class*, Fig. 7a). S is mostly anti-correlated with or precedes Q (*Preceding class* or *Anti-phase class*, Fig. 7a).

355 During the melt season 2022, we observe a shift from linear responses of R and S (*In-phase class* and *Anti-phase class*, Fig. 7c) towards more hysteretic responses (*Preceding class* and *Lagging class*, Fig. 7c) when Q shows the first significant increase in June (Fig. 7c and d, ⑥). R varies with changes in Q before this event (*In-phase class*, Fig. 7c) but after, R lags behind Q (*Lagging class*, Fig. 7c). Similarly, S shifts regimes from being anti-correlated with Q before the episode ⑥ (*Anti-phase class* , Fig. 7c) to a regime where S precedes Q after this period (*Preceding class*, Fig. 7c).

360 ## 5   Discussion

5.1   Interpreting the evolution of subglacial conditions

In this study, we have analyzed variations in subglacial hydro-mechanical conditions, i.e., the response of subglacial variables to changes in runoff and interpret now the observed behavior in terms of subglacial drainage system evolution (Sec. 5.2) and till rheology (Sec. 5.3). We divided the phase relationships observed between different subglacial variables (the force, F, the

365 water pressure, p, the hydraulic gradient, S, and the hydraulic radius, R) and runoff, Q, into four classes (Fig. 2). Here, we first consider the expected responses of R, S and p to changes in Q for different typical stages of subglacial channel evolution. In

addition, we discuss expected responses of F for different till rheologies. Second, we apply this interpretation scheme to the observed behavior separately for each of the considered time scales, before we consolidate these interpretations into a coherent picture of subglacial conditions.

370   Due to the relatively low bed slope and the long distance between our borehole location and the glacier front, unpressurized drainage is unlikely to persist in these conditions and open flowpaths are expected to close quickly (Nye, 1976). For a drainage axis with a fixed cross sectional area (rigid pipe), an increase in runoff Q results in increasing water pressure p that translates to a positive, linear $p - Q$ relationship (*In-phase class*, Fig. 2). In this situation, we expect constant R, unaffected by variations in Q (not classified). Since we always measure p at the same location and the glacier terminus is fixed at sea-level, for a

375   spatially homogeneous drainage system, we expect that variations in S are closely related to those of p. However, spatio-temporal complexity in the drainage system downstream of our borehole may lead to incoherent relations between local p and spatially integrated S. According to Röthlisberger's theory for ice-walled channels (Röthlisberger, 1972), the channel cross-section is determined by the counter-acting processes of melt opening due to dissipation of potential energy and creep-closure of the surrounding ice. In steady-state, these two processes balance each other, and a larger runoff would be associated with

380   a larger channel, thus requiring lower S and p (Schoof, 2010; Werder et al., 2013). This inverse $p - Q$ relationship is one of the best-known characteristics of ice-walled drainage. Hence, we interpret a negative, linear relationship (*Anti-phase class*, Fig. 2) between Q and p (and similar for S and Q), as indicative for steady-state drainage of a preferential drainage axis. This situation also entails that R increases with Q (*In-phase class*, Fig. 2). The evolution of the drainage system in response to Q typically is transient between the two end-members described above, with a fixed cross sectional area referred to as rigid pipe

385   on one hand, and a steady-state channel on the other one. For transient evolution between these two end-members, we expect a hysteretic behavior in the phase relationships between subglacial variables and Q. Evolution towards steady-state occurs with some time delay; if variations of the forcing term Q occur faster than this delay, the variations of R lag the variation of Q, resulting in a counter-clockwise hysteresis (*Lagging class*, Fig. 2). For such a transient evolution, R is smaller during the rising limb of Q than during the decline, emanating as a counter-clockwise $R - Q$ hysteresis (*Lagging class*, Fig. 2). At the

390   same time, the larger R during the decline of Q requires a lower p to drive the flow, resulting in a clockwise hysteresis in the $p - Q$ relation (*Preceding class*, Fig. 2). As stated above, we expect S to vary in a similar fashion as p. The response of turbulent-water-flow-induced seismic power P to changes in Q is complex because it integrates the responses of both R and S, hence direct interpretation of the $P - Q$ relations is difficult (Gimbert et al., 2016; Nanni et al., 2020).

We explore two different assumptions for the interpretation of F variations experienced by the ploughmeter, following

395   Fischer and Clarke (1994) and Kavanaugh and Clarke (2006). For a Coulomb-plastic till (Iverson et al., 1998), the shear strength depends directly on the pore-water pressure, which we assume to co-vary with p at the bottom of the borehole. This behavior results in a negative, linear response of F to variations in p (*Anti-phase class*, Fig. 2). For a a linear-viscous type till (Alley, 1990; Kamb and Engelhardt, 1991) F increases linearly with sliding velocity. Usually, glacier sliding laws acknowledge a water pressure control on sliding speed (Iken and Bindschadler, 1986; Hooke et al., 1997; Zoet and Iverson, 2020; Gilbert

400   et al., 2022) which would result in a positive, linear relationship between F and p (*In-phase class*, Fig. 2). However, more complex $F - p$ relationships can emanate as well, accounting for that the relationship between p and sliding speed may be non-

linear (Alley, 1989; Boulton and Hindmarsh, 1987). In general, interpreting a direct relation between F and Q is complicated by the circumstance that variations in p (and S) also depend on the efficiency of the drainage system to evolve to cope with runoff input, hence depend both on Q and R.

Our interpretation scheme described here lets us expect two to three options for the classification of phase relations between each subglacial variable and Q. For $p - Q$ and $S - Q$, we expect behaviors according to *Preceding class*, *In-phase class* or *Anti-phase class*; we expect $R - Q$ to display either *Lagging class* or *In-phase class* behavior; $F - p$ is expected to fall either in *In-phase class* or *Anti-phase class*, direct $F - Q$ relations are not easily comprehended. In practice, we observe that some events are classified outside the expected range (Figs. 5 and 7). The occurrence of such behavior may be attributed partly to artifacts introduced by the spectral filtering applied to the time series for the analysis. Although we manually checked the consistency between the unfiltered and filtered signals to remove the most apparent differences (see Section 3.5), some inconsistencies may still remain. Small shifts in timing of peaks may be amplified by normalizing the event time axis and hence lead to mis-classification of some events. In addition, the definition of the four classes is motivated by noticing that phase relations may be linearly positive or negative or exhibit some transitory stage (preceding or lagging). To account for uncertainties symptomatic for observations of natural systems, we allow some deviation from strictly linear behavior and accept RSS ≤ 2 still representing linear behavior. The choice of this threshold is motivated from visual impression of clustering of phase relations.

5.2 Subglacial drainage system evolution

The two observed melt seasons considerably differ in terms of duration and intensity (Fig. 3). Whereas in 2021, melting occurs over a relatively short period and yields low levels of water supply, in 2022, the melt season lasts longer and is characterized by higher temperatures and thus yields higher water supply rates. This difference provides the opportunity to study the evolution of the subglacial drainage system in response to very different forcing.

5.2.1 The melt season 2021: short duration and low intensity

The melt season 2021 is short (67 days) and marked by runoff usually lower than 20 m^3 s^{-1} (Fig. 3a). Applying our inter-pretation scheme to the observed responses of the water pressure p, the turbulent-water-flow-induced seismic power P, the hydraulic radius R, and the hydraulic gradient, S, yields a largely consistent picture of a subglacial drainage system that fully adapts to seasonal runoff variations: $p - Q$ exhibits clockwise hysteresis, indicative of system capacity growing with runoff (Fig. 4d); $R - Q$ variations are positively-linearly related (Fig. 4b); the $S - Q$ relationship covers only the declining phase of Q and shows an increase of S during this decline, consistent with the above interpretation (Fig. 4c). As mentioned above, due to the composite nature of turbulent-water-flow-induced seismic power, the $P - Q$ relationship is more difficult to interpret, but comparison to idealised behavior suggests that system adjustment is dominated by different mechanisms during different stages (Fig. 4a). Although all records draw the picture of a system adjusting to Q variations, there is a noteworthy difference in the interpretations of borehole measurements and those of cryoseismology records. While long-term variations of R and S suggest that the system capacity obtains an equilibrium with Q, the variations of p, measured in the borehole, indicate a

transient evolution in response to changes in Q. $p - Q$ exhibits clockwise hysteresis, indicative of system capacity growing with runoff also this in agreement with expected behavior (Fig. 4d).

The theoretical timescale of channel adjustment is usually longer (several days to weeks) than typical variations in Q (hours) (Röthlisberger, 1972). At short time scales, drainage pathways are then either overwhelmed when Q increases or partially filled when Q decreases which results in a response similar to that of a rigid pipe (fixed cross-sectional area channel) rather than that of a steady-state channel(variable cross-section determined by the balance between melt opening and creep-closure to cope with runoff variations). We therefore expect a predominance of *In-phase class* for the $p - Q$ and $S - Q$ relationships over multi-day and diurnal time scales (Fig. 5a and 7a). The multi-day classifications of $p - Q$ and $S - Q$ relationships mainly support this view by displaying *Lagging class* and *In-phase class* behaviors (Fig.5a), however on diurnal time scales (Fig. 7a), the picture is less clear. On these shorter time scales, we expect only minor variations of R, lagging those of Q (*Lagging class*). However, we observe mainly *In-phase class* behavior at both multi-day and diurnal time scales (Fig. 5a and 7a), suggesting that geometrical adjustment of the drainage system takes place already over short time scales; however this implies that the observed behaviors of p and S are caused by changes in hydraulic roughness since R already has adjusted.

Towards the end of the melt season 2021, a major rainfall event (Fig. 3, ③) left a clear impact on p at the multi-day time scale (Fig. 3d, Fig. 5a) and coincided with a considerable glacier acceleration. During this event, the $p - Q$ relationship indicates that the drainage system evolves in a transient manner (*In-phase class*, Fig. 5a). Prior to this event, Q was at low levels for a period of about 10 days (Fig. 3d), and presumably, the capacity of the drainage system had decreased, when it suddenly became overwhelmed by the arrival of water volumes. This results in a sharp increase of p, provoking a short-term acceleration of the glacier. Similar late season events have also been reported in other studies (Andrews et al., 2014; Rada and Schoof, 2018).

5.2.2 The melt season 2022: long duration and high intensity

In contrast to the melt season 2021, the melt season 2022 is long (at least, 83 days since our records end before the melt season ceases) and contains frequent and large excursions of runoff Q above 20 m^3 s^{-1} (Fig. 3a) leading to a different evolution of the subglacial drainage system compared to the preceding year. The $R - Q$ relationship is linearly positive, indicating drainage system size evolving at equilibrium with Q (Fig. 4g). The $S - Q$ relationship follows a trajectory that first is typical of a steady-state channel (Fig. 4h, 1) before bending over to a positive slope similar to that expected for a rigid pipe (Fig. 4h, 2, 3 and 4). Such behavior is typical for a system that is continuously overwhelmed since the subglacial preferential drainage axes cannot adapt fast enough to increasing Q. $P - Q$ relationship in 2022 shows similar behavior as in 2021, if we account for that the 2022 record does not cover the falling limb of Q (Fig. 4f). The view of a continuously overwhelmed drainage system is further supported by the generally positive slope of the $p - Q$ relationship which has a considerably smaller clockwise hysteresis compared to the preceding year (Fig. 4i).

Over shorter time scales, the classifications of $R - Q$ and $S - Q$ exhibit similar behavior as in 2021 (Fig. 5b and 7b), indicative for system adjustment also on multi-day and diurnal times. However, the *Lagging class* behavior of $S - Q$ in the beginning of the melt season visible in Figure 5b, remains difficult to explain. On a diurnal time scale, the dominance of *Anti-phase class* in the $S - Q$ relation before July 2022 suggests that preferential drainage axis evolution is in equilibrium with Q (Fig. 7b). The

data then displays a switch to mainly *Preceding class* behavior, which in turn is indicative of a transient evolution, typical for a drainage system that cannot adapt fast enough to the runoff variations. $R - Q$ relationship exhibits a similar switch (from *In-phase class* to class II 7b) with implications consistent to the interpretation above. The *Preceding class* behavior of $p - Q$ on multi-day scales further supports the view of geometric adjustment at this scale. The same analysis on the diurnal scale (Fig. 7b) reveals that there is more diurnal variations in p during the melt season 2022, compared to 2021 (more events are classified). However, the diurnal analysis renders a blurry picture since all classes occur and no clear pattern can be depicted (Fig. 3d).

5.2.3 Ambiguous interpretation from borehole and cryoseismic records

In the previous section, we interpreted the multi-variable record in terms of drainage system evolution in response to runoff (summarised in Figure 9). We note that sometimes, interpretations derived from different records are ambiguous. For instance, during the melt season 2021, on a seasonal scale the relationships between the cryoseismic record (P) and derived variables (R and S) and Q yield a picture of a subglacial drainage system in equilibrium with Q. In contrast, the $p - Q$ relationship based on the borehole record is symptomatic of a transient evolution where geometric adjustments lag variations in Q. Another example is found in the analysis of diurnal variations in 2022 (Fig. 7b) where the cryoseismic records indicate a switch from an equilibrium to a transient evolution coinciding with a major increase in Q (Fig. 7d ⑥). The corresponding classification of the $p - Q$ relation is less conclusive about a similar switch and exhibits variations over all classes with no clearly recognizable pattern. In this section, we discuss potential sources for these inconsistencies and how these may be resolved.

Perceiving the drainage system as a macroporous sheet goes along with the spatial heterogeneity of the subglacial drainage system, with parts of the glacier base being located in areas that are well connected to the main water drainage, whereas other parts only indirectly communicate with that system (Murray and Clarke, 1995; Rada and Schoof, 2018), for instance through a porous medium of lower permeability. Such a situation would apply when interpreting records from sensors that are physically installed at different locations along the base (e.g., in different boreholes), but also, when the view-field of the individual sensors differs such that the recorded signals have different characteristics of noise and signal amplitude. In our case, P integrates the seismicity in the 3-10 Hz frequency band in which seismic wavelengths are on the order of 150-500m (for typical surface wave velocity on the order of $1500 \ \mathrm{m \ sec^{-1}}$ Köhler et al., 2012; Gimbert et al., 2021b). Accordingly, the cryoseismologically derived variables P, R and S are sensitive to an area of $\sim 1 \ \mathrm{km^2}$ around the geophone location, and therefore, they will always represent the hydraulically most active part within this area (Nanni et al., 2021).

In contrast, water pressure p is measured at the bottom of the borehole, the precise dimensions of which at the base of the glacier are unknown, but estimated to be $\sim 20 \ \mathrm{cm}$ in diameter. Depending on the hydraulic connection of the borehole and the ice-till coupling, p may be representative for about $1 \ \mathrm{m^2}$ in case of hydraulic isolation, or for a several orders of magnitude larger area in case of a direct connection to a preferential drainage axis (Murray and Clarke, 1995; Mair et al., 2001, 2003). In addition, the hot-water drilling operation might have disturbed the subglacial environment (excavation of fines, volume of water pushed to the bed), influencing the water pressure observation. However, the volume of water injected through hydraulic connection of the borehole to the bed is limited ($\sim 0.5 \ \mathrm{m^3}$ for the observed 30 m drop of water column at connection) and the

borehole has been drilled beginning of May 2021. In the absence of surface melting before late June 2021, it seems unlikely that a potential initial connection could be maintained. Geometrically controlled patterns of channelization on a hard bed may be persistent, but a soft sediment bed provides less geometrical controls on the spatial patterns and year-to-year variability of channel location within a few meters seems plausible. In addition, several studies report that water pressure records displayed regime changes and suggest that these may reflect reorganization of the drainage system (Gordon et al., 1998; Kavanaugh and Clarke, 2000; Schuler et al., 2002; Andrews et al., 2014; Rada and Schoof, 2018). Resuming the idea of a spatially heterogeneous and discontinuous drainage system aids resolving the apparent discrepancies derived from the different records: if the active drainage system within 1 km^2 around our instrument site is in equilibrium with Q, the seismological record would reveal this effect, whereas the borehole record may reveal a different interpretation if the borehole itself is located in a less-well connected or even isolated part of the glacier bed. The apparent discrepancy derived from different records therefore supports the comprehension of the drainage system as a discontinuous, spatially heterogeneous sheet. Although the minor diurnal variability of p during the melt season 2022 may be interpreted as symptomatic for hydraulic isolation, p displays seasonal variability responding to Q. This observation suggests that differently connected parts of the glacier bed hydraulically communicate, at least when the capacity of the drainage system is overwhelmed in times of high water supply. Sufficiently high water pressure in connected bed areas can cause the expansion of the connected drainage system (Murray and Clarke, 1995). During such episodes, high water pressures would occur over a large part of the glacier bed, possibly promoting glacier sliding. Indeed, during the melt season 2022, several episodes of glacier acceleration are recorded during episodes of high Q that coincided with p close to overburden pressure (Fig. 3 b ⑥, ⑦), even though the borehole was not well connected to the main drainage system. Conversely, when the connected areas of the bed operate at low water pressure, areas of the bed adjacent to the preferential drainage axes are hydraulically isolated by stress-bridging (Lappegard et al., 2006), resulting in areas of the glacier bed switching back and forth between connected and isolated (Murray and Clarke, 1995).

5.3 Till changes and glacier dynamics

In the Section 5.1 above, we have proposed an interpretation scheme based on the phase relationship between the force experienced by the ploughmeter, F, and the pore water pressure of the till, here taken as adequately represented by p. In this section, we explore subglacial processes that may explain the complex relationship observed between the subglacial hydrology (represented by the subglacial water pressure) and the mechanical properties of the till (represented by the force experienced by the ploughmeter) assuming a Coulomb-plastic rheology. We recall that for such a constitutive flow law for the till, a negative $p - F$ relationship is expected (*In-phase class*).

Over a seasonal scale during the melt seasons, the $p - F$ relation displays a generally negative slope (Figs. 4e and j and 8a). For a Coulomb-plastic material, an increase in pore water pressure results in a decrease in shear strength, which in turn would cause a decrease in F (Fig. 9). Furthermore, the observed anti-correlation between p and F is in good agreement with the modeling results of Kavanaugh and Clarke (2006) for a Coulomb-plastic material, an interpretation that is in line with the findings of Fischer and Clarke (1994); Fischer et al. (1998, 2001) at Trapridge glacier, Storglaciären and Unteraargletscher, respectively. However, during winter 2021/22, the $p - F$ relationship exhibits a positive slope (Fig. 8a) which is unexpected for
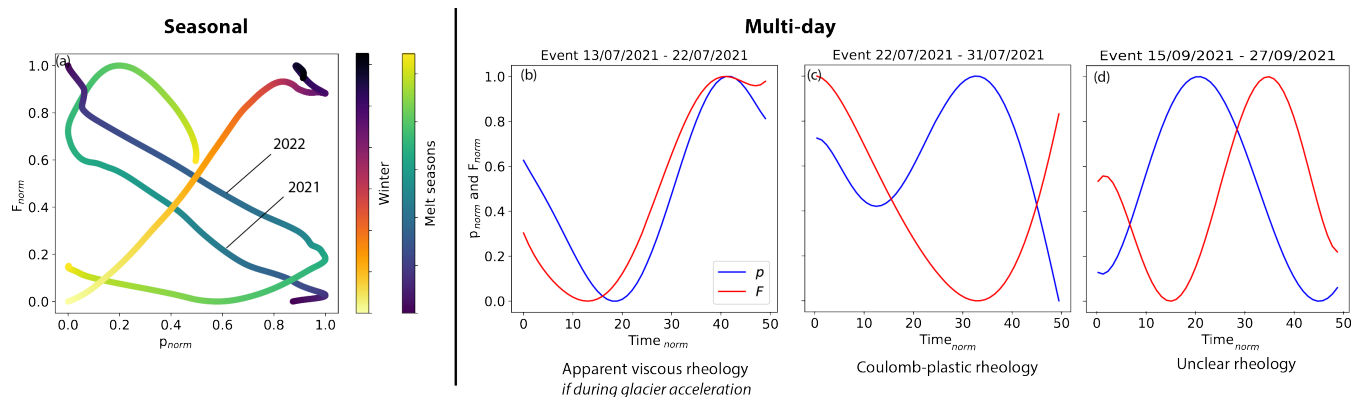
Figure 8. Comparison between the variations of water pressure p and ploughmeter force F (a) at the seasonal, and (b) to (d) multi-day time scales. (a) Relationship between p and F at the seasonal time scale. F and p are normalised (min-max normalisation) to be comparable. Blue-yellow and yellow-purple color scales indicate time during melt seasons and winter, respectively. (b) Evolutions of F (red) and p (blue) for an event indicative of apparent viscous behavior (assuming that p is positively related to basal motion). Similar behaviour has been observed also during other periods (e.g., from July 13, 2021 to July 22, 2021, and August 8, 2021 to August 17, 2021). The time of the event is normalised over 50 time steps. (c) Evolutions of F (red) and p (blue) for an event indicative of Coulomb-plastic behavior. Similar behaviour has been observed also during other periods (e.g., from July 22, 2021 to July 31, 2021, from July 7, 2021 to August 8, 2021, and from July 11, 2022 to July 23, 2022). The time of the event is normalised over 50 time steps. (d) Evolutions of F (red) and p (blue) that remain unclear as the interpretation scheme does not provide a clear indication of till rheology. Similar behaviour has been observed also during other periods (e.g., from September 15, 2021 to September 27, 2021, and from May 28, 2022 to June 6, 2022). The time of the event is normalised over 50 time steps. Simultaneous multi-day variations of F and p can be assessed only for five and two events during the melt seasons 2021 and 2022, respectively. All panels show normalized variations of F and p.

Coulomb-plastic rheology. Apparent-viscous behavior entails a velocity dependency of basal resistance, resulting in a positive $p - F$ relationship. However, we do not observe glacier acceleration during the same period in winter 2021/22.

Over shorter time scales, time series of p and F exhibit complex behavior: correlation (Fig. 8b), anti-correlation (Fig. 8c), and lagging after each configuration other occur (Fig. 8d). Applying our interpretation scheme suggests that during episodes similar to those displayed in Figure 8c, the inverse $p - F$ correlation results from weakening of the sediment at times of high water pressure due to reduced effective pressure and vice versa, as expected for a near-Coulomb rheology (Fig. 9). However, a positive relationship between p and F as pictured in Figures 8b and d does not agree with Coulomb-plastic rheology. The illustrated episodes apparently do not coincide with periods of high surface velocity. Similar $p - F$ correlations have been observed previously (e.g., Murray and Porter, 2001; Rousselot and Fischer, 2007; Thomason and Iverson, 2008) but not extensively discussed. A range of mechanisms have been proposed to explain such behavior, such as the sediments loaded towards their yield point (e.g., Murray and Porter, 2001), the state of the mechanical coupling between the ice and the till and its influence on pore-pressure variations (Iverson et al., 1995; Fischer and Clarke, 1997; Boulton et al., 2001; Mair et al., 2003; Iverson, 2010), the varying mobilisation of the till at depth (e.g., Iverson et al., 1998; Tulaczyk, 1999; Tulaczyk et al., 2001;

Truffer et al., 2000; Truffer, 2004). However, a direct explanation on how these mechanisms would explain the correlation between F and p is not straightforward. We further point out that the attitude of the ploughmeter relative to the till may have changed, for instance through changes in tilt or vertical position, but these effects cannot be disentangled from till behavior without further accompanying measurements. Such measurements will be subject for future ploughmeter deployments.

6 Conclusions

In this study, we adopt a multi-method, multi-scale analysis to examine the responses of the subglacial environment of the Kongsvegen glacier, Svalbard, to changes in runoff. We synthesize the broad spectrum of sediment deformation and subglacial drainage behaviors in four classes and interpret them in terms of drainage system evolution and till rheology (Fig. 9).

Our data cover two contrasting melt seasons: during the short and less intensive melt season 2021, we conjecture that our borehole intersected a well-connected part of the subglacial drainage system, whereas in the longer and intensive melt season 2022, the borehole recorded characteristics of a poorly connected subdomain of the glacier bed (Fig. 9). Seismological records indicate the existence of an efficient drainage system in both periods. Considering the different footprints of our sensors (e.g., meter-scale sensitivity for the ploughmeter and the water pressure sensor and hundreds of meter-scale sensitivity for the seismic investigation due to the selected frequencies), complementary information can be obtained that allows us to propose a consistent picture of the subglacial environment. We therefore suggest the co-existence of efficient and inefficient drainage system components together with isolated patches, rendering the perception of a discontinuous, spatially heterogeneous drainage system (Fig. 9, Rada Giacaman and Schoof, 2023).

The relationship between the force experienced by the ploughmeter and the water pressure reveals complex till rheology. As expected, the till behaves mainly as a Coulomb-plastic material but episodically, the $p - F$ relation is indicative of deviating behavior. Such behavior may be caused by different mechanisms, e.g. till loading towards its yield strength, or variations in the mobilization of the till at depth, but we cannot exclude possible effects of changes in instrument-till coupling that may cause similar behavior. In future, additional measurements of instrument attitude could help disentangling instrument behavior from till behavior and assessments of changes in till properties using seismic noise interferometry (Zhan, 2019) over a large area could complement the local ploughmeter record.

In this study, we show the importance of a multi-sensor multi-scale approach to study the complex variations of hydro-mechanical conditions in response to runoff changes. Such an approach may also be beneficial for studying the dynamics of other transient geological systems that are characterized by build-up and evolution of internal states. These states may reach critical thresholds causing instabilities over different scales from short-lived events to large-scale by destabilization as exemplified in many geohazards such as glacial surges or collapses, volcanic eruptions, landslides, or earthquakes.
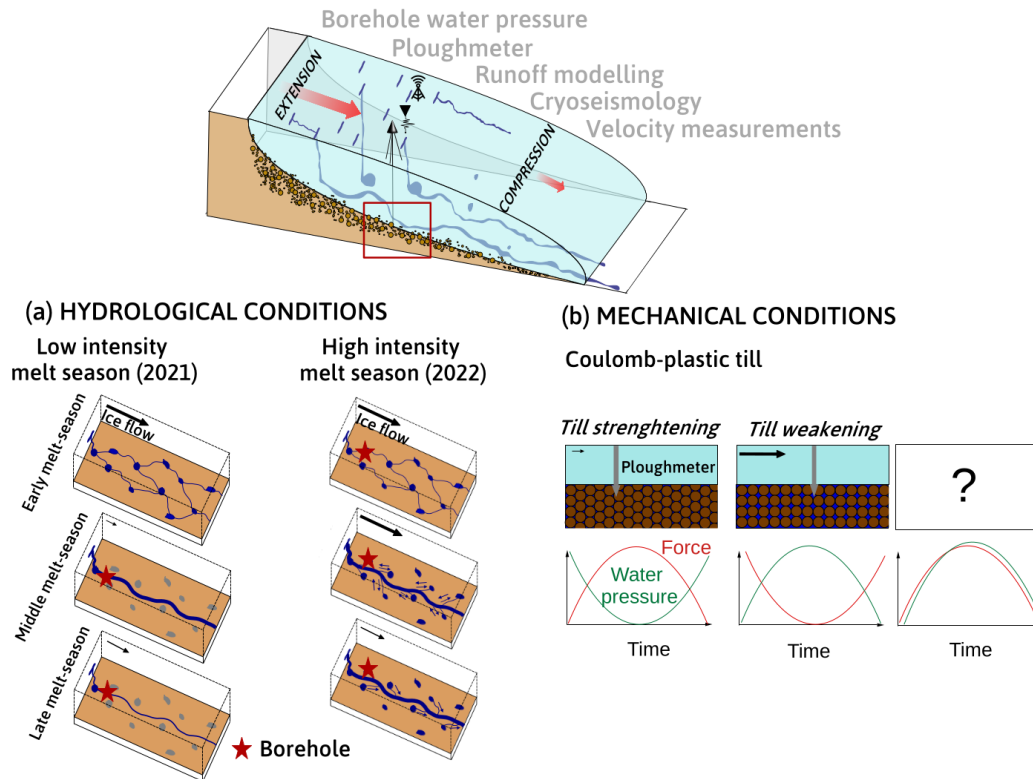
Figure 9. Sketch of the adjustment of hydro-mechanical conditions below Kongsvegen glacier to variations in runoff over the period from June 2021 to August 2022. (a) Hydraulic quantities, i.e. water pressure (p), hydraulic gradient (S), and hydraulic radius (R), used to characterize the evolution of the subglacial drainage system during the short and low intensity melt season of 2021, and the long and high intensity melt season of 2022. Our findings indicate that during the 2021 season, the subglacial drainage system adapted to runoff changes in steady-state, leading to an increase in its capacity over time. However, during the 2022 season, we observed a transient evolution of the drainage system in response to the continued and high-intensity input of runoff. As a result, the drainage capacity of the main drainage system was exceeded, causing water to leak into poorly connected areas of the bed increasing the water pressure, thereby triggering speed-up events. (b) The mechanical quantity, i.e., force (F), was used to examine the rheological behavior of the till. The till rheology behaved mainly as a Coulomb-plastic material (anti-correlation between p and F), but episodically showed deviating behavior (correlation between p and F), the underlying mechanisms for which remain unclear.

Code and data availability. The data are uploaded in Zenodo (https://doi.org/10.5281/zenodo.7648444, Bouchayer (2023a)) and the code to reproduce the figures in the manuscript can be found on GitHub (https://github.com/Colinebouch/mammamia_alldata_processing, Bouchayer (2023b)).

Author contributions. CB, UN and TVS designed the concept of the study. CB developed the code, produced all tables and figures and wrote the initial draft. UN and TVS provided help and ideas in all phases of the study and wrote parts of the manuscript. FR provided ideas and feedbacks that lead to the finalisation of the manuscript. TVS provided all the organizational and technical support. JK and TVS provided the logistical support to conduct the field campaigns. JH built the ploughmeter. CB, UN, JH, TVS, PML and JK conducted fieldwork. TVS and CB processed the ploughmeter and water pressure data. UN and CB processed the seismic data. PML processed the GNSS velocity data. JK provided the long term velocity data at KNG6. LS contributed with CARRA and AROME-ARCTIC forcing, and simulated surface runoff. All authors contributed to the final manuscript with input and suggestions.

Competing interests. The authors declare no conflict of interest.

Acknowledgements. This project has received support from the Research Council of Norway through the projects MAMMAMIA (grant no. 301837) and SLIDE (no. 337228) and from the Faculty of Mathematics and Natural Sciences at the University of Oslo through the strategic research initiative EarthFlows. TVS and FR acknowledge support from the project FricFrac funded by the Center for Advanced Study (CAS) at the Norwegian Academy of Science and Letters during academic year 2023-2024. We are grateful to the Governor of Svalbard for permitting fieldwork at Kongsvegen. The energetic help of Wenxue Cao, Ceslav Czyk, Basile De Fleurian, Jean-Charles Gallet, Adrien Gilbert, Stephen Hudson, Simon Filhol, Urs Fischer, Catherine Larose, and Ashley Morris during the field campaigns is greatly acknowledged. UN acknowledges Andreas Köhler for support in the seismic data analysis. We thank the editor, Prof. Elisa Mantelli, and two anonymous reviewers for thorough reviews that greatly improved an earlier version of the manuscript.

References

Alley, R.: Water-pressure coupling of sliding and bed deformation: II. Velocity-depth profiles, Journal of Glaciology, 35, 119–129, 1989.

Alley, R. B.: Multiple steady states in ice-water-till systems, Annals of Glaciology, 14, 1–5, 1990.

Andrews, L. C., Catania, G. A., Hoffman, M. J., Gulley, J. D., Lüthi, M. P., Ryser, C., Hawley, R. L., and Neumann, T. A.: Direct observations of evolving subglacial drainage beneath the Greenland Ice Sheet, Nature, 514, 80–83, 2014.

Bælum, K. and Benn, D.: Thermal structure and drainage system of a small valley glacier (Tellbreen, Svalbard), investigated by ground penetrating radar, The Cryosphere, 5, 139–149, 2011.

Bartholomaus, T. C., Amundson, J. M., Walter, J. I., O'Neel, S., West, M. E., and Larsen, C. F.: Subglacial discharge at tidewater glaciers revealed by seismic tremor, Geophysical research letters, 42, 6391–6398, 2015.

Benn, D., Gulley, J., Luckman, A., Adamek, A., and Glowacki, P. S.: Englacial drainage systems formed by hydrologically driven crevasse propagation, Journal of Glaciology, 55, 513–523, 2009.

Benn, D., Fowler, A. C., Hewitt, I., and Sevestre, H.: A general theory of glacier surges, Journal of Glaciology, 65, 701–716, 2019.

Beyreuther, M., Barsch, R., Krischer, L., Megies, T., Behr, Y., and Wassermann, J.: ObsPy: A Python toolbox for seismology, Seismological Research Letters, 81, 530–533, 2010.

Björnsson, H., Gjessing, Y., Hamran, S.-E., Hagen, J. O., LiestøL, O., Pálsson, F., and Erlingsson, B.: The thermal regime of sub-polar glaciers mapped by multi-frequency radio-echo sounding, Journal of Glaciology, 42, 23–32, 1996.

Bouchayer, C.: Dataset at a 3h resolution used in the paper 'The MAMMAMIA project: A multi-scale multi- method approach to understand runoff-induced changes in the subglacial environment and consequences for surge dynamic in Kongsvegen glacier, Svalbard', https://doi.org/10.5281/zenodo.7648444, 2023a.

Bouchayer, C.: GitHub repository to process the data, published in Zenodo, https://github.com/Colinebouch/mammamia_alldata_processing/commits/v1.0, https://doi.org/10.5281/zenodo.7648470, last update: 17/02/2022, 2023b.

Boulton, G. and Hindmarsh, R.: Sediment deformation beneath glaciers: rheology and geological consequences, Journal of Geophysical Research: Solid Earth, 92, 9059–9082, 1987.

Boulton, G., Dobbie, K., and Zatsepin, S.: Sediment deformation beneath glaciers and its coupling to the subglacial hydraulic system, Quaternary International, 86, 3–28, 2001.

Clarke, G. K.: Subglacial processes, Annu. Rev. Earth Planet. Sci., 33, 247–276, 2005.

Clyne, E., Alley, R. B., Vore, M., Gräff, D., Anandakrishnan, S., Walter, F., and Sergeant, A.: Glacial hydraulic tremor on Rhonegletscher, Switzerland, Journal of Glaciology, 69, 370–380, 2023.

Creyts, T. T. and Schoof, C. G.: Drainage through subglacial water sheets, Journal of Geophysical Research: Earth Surface, 114, 2009.

Damsgaard, A., Egholm, D. L., Piotrowski, J. A., Tulaczyk, S., Larsen, N. K., and Tylmann, K.: Discrete element modeling of subglacial sediment deformation, Journal of Geophysical Research: Earth Surface, 118, 2230–2242, 2013.

Damsgaard, A., Egholm, D. L., Beem, L. H., Tulaczyk, S., Larsen, N. K., Piotrowski, J. A., and Siegfried, M. R.: Ice flow dynamics forced by water pressure variations in subglacial granular beds, Geophysical Research Letters, 43, 12–165, 2016.

Damsgaard, A., Goren, L., and Suckale, J.: Water pressure fluctuations control variability in sediment flux and slip dynamics beneath glaciers and ice streams, Communications Earth & Environment, 1, 66, 2020.

De Fleurian, B., Gagliardini, O., Zwinger, T., Durand, G., Le Meur, E., Mair, D., and Råback, P.: A double continuum hydrological model for glacier applications, The Cryosphere, 8, 137–153, 2014.

Doyle, S. H., Hubbard, B., Christoffersen, P., Young, T. J., Hofstede, C., Bougamont, M., Box, J., and Hubbard, A.: Physical conditions of fast glacier flow: 1. Measurements from boreholes drilled to the bed of Store Glacier, West Greenland, Journal of Geophysical Research: Earth Surface, 123, 324–348, 2018.

Engelhardt, H. and Kamb, B.: Basal hydraulic system of a West Antarctic ice stream: constraints from borehole observations, Journal of Glaciology, 43, 207–230, 1997.

Fischer, U. H. and Clarke, G. K.: Ploughing of subglacial sediment, Journal of Glaciology, 40, 97–106, 1994.

Fischer, U. H. and Clarke, G. K.: Stick–slip sliding behaviour at the base of a glacier, Annals of Glaciology, 24, 390–396, 1997.

Fischer, U. H., Iverson, N. R., Hanson, B., Hooke, R. L., and Jansson, P.: Estimation of hydraulic properties of subglacial till from plough-meter measurements, Journal of Glaciology, 44, 517–522, 1998.

Fischer, U. H., Clarke, G. K., and Blatter, H.: Evidence for temporally varying "sticky spots" at the base of Trapridge Glacier, Yukon Territory, Canada, Journal of Glaciology, 45, 352–360, 1999.

Fischer, U. H., Porter, P. R., Schuler, T., Evans, A. J., and Gudmundsson, G. H.: Hydraulic and mechanical properties of glacial sediments beneath Unteraargletscher, Switzerland: implications for glacier basal motion, Hydrological Processes, 15, 3525–3540, 2001.

Flowers, G. E.: Modelling water flow under glaciers and ice sheets, Proceedings of the Royal Society A: Mathematical, Physical and Engineering Sciences, 471, 20140 907, 2015.

Flowers, G. E. and Clarke, G. K.: A multicomponent coupled model of glacier hydrology 1. Theory and synthetic examples, Journal of Geophysical Research: Solid Earth, 107, ECV–9, 2002a.

Flowers, G. E. and Clarke, G. K.: A multicomponent coupled model of glacier hydrology 2. Application to Trapridge Glacier, Yukon, Canada, Journal of Geophysical Research: Solid Earth, 107, ECV–10, 2002b.

Fudge, T., Humphrey, N. F., Harper, J. T., and Pfeffer, W. T.: Diurnal fluctuations in borehole water levels: configuration of the drainage system beneath Bench Glacier, Alaska, USA, Journal of Glaciology, 54, 297–306, 2008.

Gilbert, A., Gimbert, F., Thøgersen, K., Schuler, T. V., and Kääb, A.: A Consistent Framework for Coupling Basal Friction With Subglacial Hydrology on Hard-Bedded Glaciers, Geophysical Research Letters, 49, e2021GL097 507, 2022.

Gillet-Chaulet, F., Durand, G., Gagliardini, O., Mosbeux, C., Mouginot, J., Rémy, F., and Ritz, C.: Assimilation of surface velocities acquired between 1996 and 2010 to constrain the form of the basal friction law under Pine Island Glacier, Geophysical Research Letters, 43, 10–311, 2016.

Gimbert, F., Tsai, V. C., Amundson, J. M., Bartholomaus, T. C., and Walter, J. I.: Subseasonal changes observed in subglacial channel pressure, size, and sediment transport, Geophysical Research Letters, 43, 3786–3794, 2016.

Gimbert, F., Gilbert, A., Gagliardini, O., Vincent, C., and Moreau, L.: Do existing theories explain seasonal to multi-decadal changes in glacier basal sliding speed?, Geophysical Research Letters, 48, e2021GL092 858, 2021a.

Gimbert, F., Nanni, U., Roux, P., Helmstetter, A., Garambois, S., Lecointre, A., Walpersdorf, A., Jourdain, B., Langlais, M., Laarman, O., et al.: A multi-physics experiment with a temporary dense seismic array on the Argentière glacier, French Alps: The RESOLVE project, Seismological Society of America, 92, 1185–1201, 2021b.

Goldberg, D., Schoof, C., and Sergienko, O.: Supporting Material for Stick-slip motion of an Antarctic Ice Stream: the effects of viscoelasticity, 2014.

Gordon, S., Sharp, M., Hubbard, B., Smart, C., Ketterling, B., and Willis, I.: Seasonal reorganization of subglacial drainage inferred from measurements in boreholes, Hydrological Processes, 12, 105–133, 1998.

Gräff, D., Köpfli, M., Lipovsky, B. P., Selvadurai, P. A., Farinotti, D., and Walter, F.: Fine structure of microseismic glacial stick-slip, Geophysical Research Letters, 48, e2021GL096 043, 2021.

Gulley, J.: Structural control of englacial conduits in the temperate Matanuska Glacier, Alaska, USA, Journal of Glaciology, 55, 681–690, 2009.

675 Hagen, J. O., Liestøl, O., Roland, E., and Jørgensen, T.: Glacier atlas of Svalbard and jan mayen, vol. 129, Norsk Polarinstitutt Oslo, 1993.

Hansen, D. and Zoet, L.: Characterizing sediment flux of deforming glacier beds, Journal of Geophysical Research: Earth Surface, 127, e2021JF006 544, 2022.

Hjelle, A.: Geology of Svalbard, 1993.

Hoffman, M. J., Andrews, L. C., Price, S. F., Catania, G. A., Neumann, T. A., Lüthi, M. P., Gulley, J., Ryser, C., Hawley, R. L., and Morriss,

680 B.: Greenland subglacial drainage evolution regulated by weakly connected regions of the bed, Nature communications, 7, 13 903, 2016.

Hoffmann, K.: Applying the wheatstone bridge circuit, HBM Germany, 1974.

Hooke, R. L., Laumann, T., and Kohler, J.: Subglacial water pressures and the shape of subglacial conduits, Journal of Glaciology, 36, 67–71, 1990.

Hooke, R. L., Hanson, B., Iverson, N. R., Jansson, P., and Fischer, U. H.: Rheology of till beneath Storglaciären, Sweden, Journal of

685 Glaciology, 43, 172–179, 1997.

Hubbard, B., Sharp, M., Willis, I., Nielsen, M., and Smart, C.: Borehole water-level variations and the structure of the subglacial hydrological system of Haut Glacier d'Arolla, Valais, Switzerland, Journal of Glaciology, 41, 572–583, 1995.

Hudson, T., Kufner, S., Brisbourne, A., Kendall, J., Smith, A., Alley, R., Arthern, R., and Murray, T.: Highly variable friction and slip observed at Antarctic ice stream bed, Nature Geoscience, pp. 1–7, 2023.

690 Humphrey, N., Kamb, B., Fahnestock, M., and Engelhardt, H.: Characteristics of the bed of the lower Columbia Glacier, Alaska, Journal of Geophysical Research: Solid Earth, 98, 837–846, 1993.

Iken, A.: The effect of the subglacial water pressure on the sliding velocity of a glacier in an idealized numerical model, Journal of Glaciology, 27, 407–421, 1981.

Iken, A. and Bindschadler, R. A.: Combined measurements of subglacial water pressure and surface velocity of Findelengletscher, Switzer-

695 land: conclusions about drainage system and sliding mechanism, Journal of Glaciology, 32, 101–119, 1986.

Iken, A. and Truffer, M.: The relationship between subglacial water pressure and velocity of Findelengletscher, Switzerland, during its advance and retreat, Journal of Glaciology, 43, 328–338, 1997.

IPCC: Special Report on the Ocean and Cryosphere in a Changing Climate [H.-O. Pörtner, D.C. Roberts, V. Masson-Delmotte, P. Zhai, M. Tignor, E. Poloczanska, K. Mintenbeck, A. Alegría, M. Nicolai, A. Okem, J. Petzold, B. Rama, N.M. Weyer (eds.)], vol. In Press,

700 Cambridge University Press, Cambridge, United Kingdom and New York, NY, USA, https://doi.org/10.1017/9781009157964., 2019.

Irvine-Fynn, T. D., Hodson, A. J., Moorman, B. J., Vatne, G., and Hubbard, A. L.: Polythermal glacier hydrology: A review, Reviews of Geophysics, 49, 2011.

Iverson, N. R.: Shear resistance and continuity of subglacial till: hydrology rules, Journal of Glaciology, 56, 1104–1114, 2010.

Iverson, N. R. and Iverson, R. M.: Distributed shear of subglacial till due to Coulomb slip, Journal of Glaciology, 47, 481–488, 2001.

705 Iverson, N. R., Jansson, P., and Hooke, R. L.: In-situ measurement of the strength of deforming subglacial till, Journal of Glaciology, 40, 497–503, 1994.

Iverson, N. R., Hanson, B., Hooke, R. L., and Jansson, P.: Flow mechanism of glaciers on soft beds, Science, 267, 80–81, 1995.

Iverson, N. R., Hooyer, T. S., and Baker, R. W.: Ring-shear studies of till deformation: Coulomb-plastic behavior and distributed strain in glacier beds, Journal of Glaciology, 44, 634–642, 1998.

710 Iverson, N. R., Hooyer, T. S., Fischer, U. H., Cohen, D., Moore, P. L., Jackson, M., Lappegard, G., and Kohler, J.: Soft-bed experiments beneath Engabreen, Norway: regulation infiltration, basal slip and bed deformation, Journal of Glaciology, 53, 323–340, 2007.

Javed, A., Hamshaw, S. D., Lee, B. S., and Rizzo, D. M.: Multivariate event time series analysis using hydrological and suspended sediment data, Journal of Hydrology, 593, 125 802, 2021.

Kamb, B.: Glacier surge mechanism based on linked cavity configuration of the basal water conduit system, Journal of Geophysical Research:

715 Solid Earth, 92, 9083–9100, 1987.

Kamb, B.: Basal zone of the West Antarctic ice streams and its role in lubrication of their rapid motion, The West Antarctic ice sheet: behavior and environment, 77, 157–199, 2001.

Kamb, B. and Engelhardt, H.: Antarctic ice stream B: conditions controlling its motions and interactions with the climate system, IAHS Publication, 208, 145–154, 1991.

720 Kavanaugh, J. L. and Clarke, G. K.: Evidence for extreme pressure pulses in the subglacial water system, Journal of Glaciology, 46, 206–212, 2000.

Kavanaugh, J. L. and Clarke, G. K.: Discrimination of the flow law for subglacial sediment using in situ measurements and an interpretation model, Journal of Geophysical Research: Earth Surface, 111, 2006.

Köhler, A., Chapuis, A., Nuth, C., Kohler, J., and Weidle, C.: Autonomous detection of calving-related seismicity at Kronebreen, Svalbard,

725 The Cryosphere, 6, 393–406, 2012.

Köhler, A., Nuth, C., Schweitzer, J., Weidle, C., and Gibbons, S. J.: Regional passive seismic monitoring reveals dynamic glacier activity on Spitsbergen, Svalbard, Polar Research, 34, 26 178, 2015.

Köpfli, M., Gräff, D., Lipovsky, B. P., Selvadurai, P. A., Farinotti, D., and Walter, F.: Hydraulic Conditions for Stick-Slip Tremor Beneath an Alpine Glacier, Geophysical Research Letters, 49, e2022GL100 286, 2022.

730 Labedz, C. R., Bartholomaus, T. C., Amundson, J. M., Gimbert, F., Karplus, M. S., Tsai, V. C., and Veitch, S. A.: Seismic mapping of subglacial hydrology reveals previously undetected pressurization event, Journal of Geophysical Research: Earth Surface, 127, e2021JF006 406, 2022a.

Labedz, C. R., Bartholomaus, T. C., Amundson, J. M., Karplus, M. S., Veitch, S. A., and Shugar, D. H.: Swarm-Like Behavior of Icequakes Associated with Surface Crevassing Activity on a Mountain Glacier, in: AGU Fall Meeting Abstracts, vol. 2022, pp. NS43A–04, 2022b.

735 Lappegard, G., Kohler, J., Jackson, M., and Hagen, J. O.: Characteristics of subglacial drainage systems deduced from load-cell measurements, Journal of Glaciology, 52, 137–148, https://doi.org/10.3189/172756506781828908, 2006.

Liestøl, O.: The glaciers in the Kongsfjorden area, Spitsbergen, Norsk Geografisk Tidsskrift-Norwegian Journal of Geography, 42, 231–238, 1988.

Lindner, F., Walter, F., Laske, G., and Gimbert, F.: Glaciohydraulic seismic tremors on an Alpine glacier, The Cryosphere, 14, 287–308,

740 2020.

Lliboutry, L.: General theory of subglacial cavitation and sliding of temperate glaciers, Journal of Glaciology, 7, 21–58, 1968.

Mair, D., Nienow, P., Willis, I., and Sharp, M.: Spatial patterns of glacier motion during a high-velocity event: Haut Glacier d'Arolla, Switzerland, Journal of Glaciology, 47, 9–20, 2001.

Mair, D., Willis, I., Fischer, U. H., Hubbard, B., Nienow, P., and Hubbard, A.: Hydrological controls on patterns of surface, internal and basal

745 motion during three "spring events": Haut Glacier d'Arolla, Switzerland, Journal of Glaciology, 49, 555–567, 2003.

Melvold, K. and Hagen, J. O.: Evolution of a surge-type glacier in its quiescent phase: Kongsvegen, Spitsbergen, 1964–95, Journal of Glaciology, 44, 394–404, 1998.

Minchew, B., Simons, M., Björnsson, H., Pálsson, F., Morlighem, M., Seroussi, H., Larour, E., and Hensley, S.: Plastic bed beneath Hofsjökull Ice Cap, central Iceland, and the sensitivity of ice flow to surface meltwater flux, Journal of Glaciology, 62, 147–158, 2016.

Mitchell, J. K., Soga, K., et al.: Fundamentals of soil behavior, vol. 3, John Wiley & Sons New York, 2005.

Moon, T., Ahlstrøm, A., Goelzer, H., Lipscomb, W., and Nowicki, S.: Rising oceans guaranteed: Arctic land ice loss and sea level rise, Current climate change reports, 4, 211–222, 2018.

Müller, M., Homleid, M., Ivarsson, K. I., Køltzow, M. A., Lindskog, M., Midtbø, K. H., Andrae, U., Aspelien, T., Berggren, L., Bjørge, D., Dahlgren, P., Kristiansen, J., Randriamampianina, R., Ridal, M., and Vignes, O.: AROME-MetCoOp: A nordic convective-scale operational weather prediction model, Weather and Forecasting, 32, 609–627, https://doi.org/10.1175/WAF-D-16-0099.1, 2017.

Murray, T. and Booth, A. D.: Imaging glacial sediment inclusions in 3-D using ground-penetrating radar at Kongsvegen, Svalbard, Journal of Quaternary science, 25, 754–761, 2010.

Murray, T. and Clarke, G. K.: Black-box modeling of the subglacial water system, Journal of Geophysical Research: Solid Earth, 100, 10 231–10 245, 1995.

Murray, T. and Porter, P. R.: Basal conditions beneath a soft-bedded polythermal surge-type glacier: Bakaninbreen, Svalbard, Quaternary International, 86, 103–116, 2001.

Nanni, U., Gimbert, F., Vincent, C., Gräff, D., Walter, F., Piard, L., and Moreau, L.: Quantification of seasonal and diurnal dynamics of subglacial channels using seismic observations on an Alpine glacier, The Cryosphere, 14, 1475–1496, 2020.

Nanni, U., Gimbert, F., Roux, P., and Lecointre, A.: Observing the subglacial hydrology network and its dynamics with a dense seismic array, Proceedings of the National Academy of Sciences, 118, e2023757 118, 2021.

Nanni, U., Roux, P., Gimbert, F., and Lecointre, A.: Dynamic Imaging of Glacier Structures at High-Resolution Using Source Localization With a Dense Seismic Array, Geophysical Research Letters, 49, e2021GL095 996, 2022.

Ng, F. S.: Canals under sediment-based ice sheets, Annals of Glaciology, 30, 146–152, 2000.

Nienow, P., Sole, A., Slater, D. A., and Cowton, T.: Recent advances in our understanding of the role of meltwater in the Greenland Ice Sheet system, Current Climate Change Reports, 3, 330–344, 2017.

Nye, J. F.: Water flow in glaciers: jökulhlaups, tunnels and veins, Journal of Glaciology, 17, 181–207, 1976.

Podolskiy, E. A. and Walter, F.: Cryoseismology, Reviews of geophysics, 54, 708–758, 2016.

Porter, P. R., Murray, T., and Dowdeswell, J. A.: Sediment deformation and basal dynamics beneath a glacier surge front: Bakaninbreen, Svalbard, Annals of Glaciology, 24, 21–26, 1997.

Pramanik, A., Kohler, J., Lindbäck, K., How, P., Van Pelt, W., Liston, G., and Schuler, T. V.: Hydrology and runoff routing of glacierized drainage basins in the Kongsfjord area, northwest Svalbard, The Cryosphere Discussions, pp. 1–33, 2020.

Preiswerk, L. E. and Walter, F.: High-Frequency (> 2 Hz) Ambient Seismic Noise on High-Melt Glaciers: Green's Function Estimation and Source Characterization, Journal of Geophysical Research: Earth Surface, 123, 1667–1681, 2018.

Rada, C. and Schoof, C.: Channelized, distributed, and disconnected: subglacial drainage under a valley glacier in the Yukon, The Cryosphere, 12, 2609–2636, 2018.

Rada Giacaman, C. A. and Schoof, C.: Channelized, distributed, and disconnected: spatial structure and temporal evolution of the subglacial drainage under a valley glacier in the Yukon, The Cryosphere, 17, 761–787, https://doi.org/10.5194/tc-17-761-2023, 2023.

RGI, C.: Randolph Glacier Inventory (RGI) - A dataset of Global Glacier Outlines: Version 6.0, http://www.glims.org/RGI/randolph60.html, 2017.

785 Röthlisberger, H.: Water pressure in intra-and subglacial channels, Journal of Glaciology, 11, 177–203, 1972.

Rothlisberger, H. and Lang, H.: Glacial hydrology, John Wiley & Sons, 1987.

Rounce, D. R., Hock, R., Maussion, F., Hugonnet, R., Kochtitzky, W., Huss, M., Berthier, E., Brinkerhoff, D., Compagno, L., Copland, L., et al.: Global glacier change in the 21st century: Every increase in temperature matters, Science, 379, 78–83, 2023.

Rousselot, M. and Fischer, U. H.: A laboratory study of ploughing, Journal of Glaciology, 53, 225–231, 2007.

790 Roux, P.-F., Marsan, D., Métaxian, J.-P., O'Brien, G., and Moreau, L.: Microseismic activity within a serac zone in an alpine glacier (Glacier d'Argentiere, Mont Blanc, France), Journal of Glaciology, 54, 157–168, 2008.

Schmidt, L. S., Schuler, T. V., Thomas, E. E., and Westermann, S.: Meltwater runoff and glacier mass balance in the high Arctic: 1991–2022 simulations for Svalbard, The Cryosphere, 17, 2941–2963, 2023.

Schofield, A. N. and Wroth, P.: Critical state soil mechanics, vol. 310, McGraw-hill London, 1968.

795 Scholzen, C., Schuler, T. V., and Gilbert, A.: Sensitivity of subglacial drainage to water supply distribution at the Kongsfjord basin, Svalbard, The Cryosphere, 15, 2719–2738, 2021.

Schoof, C.: The effect of cavitation on glacier sliding, Proceedings of the Royal Society A: Mathematical, Physical and Engineering Sciences, 461, 609–627, 2005.

Schoof, C.: Ice-sheet acceleration driven by melt supply variability, Nature, 468, 803–806, 2010.

800 Schuler, T., Fischer, U. H., Sterr, R., Hock, R., and Gudmundsson, G. H.: Comparison of Modeled Water Input and Measured Discharge Prior to a Release Event: Unteraargletscher, Bernese Alps, Switzerland: Selected paper from EGS General Assembly, Nice, April-2000 (Symposium OA36), Hydrology Research, 33, 27–46, 2002.

Schwanghart, W. and Scherler, D.: TopoToolbox 2 – MATLAB-based software for topographic analysis and modeling in Earth surface sciences, Earth Surface Dynamics, 2, 1–7, https://doi.org/10.5194/esurf-2-1-2014, 2014.

805 Schyberg, H., Yang, X., Køltzow, M., Amstrup, B., Bakketun, å., Bazile, E., Bojarova, J., Box, J., Dahlgren, P., Hagelin, S., Homleid, M., Horányi, A., Høyer, J., Johansson, å., Killie, M., Körnich, H., Le Moigne, P., Lindskog, M., Manninen, T., Nielsen Englyst, P., and Wang, Z.: Arctic regional reanalysis on single levels from 1991 to present, Copernicus Climate Change Service (C3S) Climate Data Store (CDS), https://doi.org/10.24381/cds.713858f6, 2020.

Sergeant, A., Yastrebov, V. A., Mangeney, A., Castelnau, O., Montagner, J.-P., and Stutzmann, E.: Numerical modeling of iceberg capsizing
810 responsible for glacial earthquakes, Journal of Geophysical Research: Earth Surface, 123, 3013–3033, 2018.

Stocker, T.: Climate change 2013: the physical science basis: Working Group I contribution to the Fifth assessment report of the Intergovernmental Panel on Climate Change, Cambridge university press, 2014.

Sugiyama, S., Skvarca, P., Naito, N., Enomoto, H., Tsutaki, S., Tone, K., Marinsek, S., and Aniya, M.: Ice speed of a calving glacier modulated by small fluctuations in basal water pressure, Nature Geoscience, 4, 597–600, 2011.

815 Sugiyama, S., Navarro, F. J., Sawagaki, T., Minowa, M., Segawa, T., Onuma, Y., Otero, J., and Vasilenko, E. V.: Subglacial water pressure and ice-speed variations at Johnsons Glacier, Livingston Island, Antarctic Peninsula, Journal of Glaciology, 65, 689–699, 2019.

Terzaghi, K., Peck, R. B., and Mesri, G.: Soil mechanics in engineering practice, John wiley & sons, 1996.

Thøgersen, K., Gilbert, A., Schuler, T. V., and Malthe-Sørenssen, A.: Rate-and-state friction explains glacier surge propagation, Nature communications, 10, 1–8, https://doi.org/10.1038/s41467-019-10506-4, 2019.

820   Thomason, J. F. and Iverson, N. R.: A laboratory study of particle ploughing and pore-pressure feedback: a velocity-weakening mechanism for soft glacier beds, Journal of Glaciology, 54, 169–181, 2008.

Truffer, M.: The basal speed of valley glaciers: an inverse approach, Journal of Glaciology, 50, 236–242, 2004.

Truffer, M., Harrison, W. D., and Echelmeyer, K. A.: Glacier motion dominated by processes deep in underlying till, Journal of Glaciology, 46, 213–221, 2000.

825   Tsai, V. C., Smith, L. C., Gardner, A. S., and Seroussi, H.: A unified model for transient subglacial water pressure and basal sliding, Journal of Glaciology, 68, 390–400, 2022.

Tulaczyk, S.: Ice sliding over weak, fine-grained tills: dependence of ice-till interactions on till granulometry, SPECIAL PAPERS-GEOLOGICAL SOCIETY OF AMERICA, pp. 159–178, 1999.

Tulaczyk, S., Kamb, W. B., and Engelhardt, H. F.: Basal mechanics of ice stream B, West Antarctica: 1. Till mechanics, Journal of Geophys-
830   ical Research: Solid Earth, 105, 463–481, 2000.

Tulaczyk, S. M., Scherer, R. P., and Clark, C. D.: A ploughing model for the origin of weak tills beneath ice streams: a qualitative treatment, Quaternary International, 86, 59–70, 2001.

Walder, J. S.: Stability of sheet flow of water beneath temperate glaciers and implications for glacier surging, Journal of Glaciology, 28, 273–293, 1982.

835   Walder, J. S.: Hydraulics of subglacial cavities, Journal of Glaciology, 32, 439–445, 1986.

Walder, J. S. and Fowler, A.: Channelized subglacial drainage over a deformable bed, Journal of glaciology, 40, 3–15, 1994.

Walker, R. T., Christianson, K., Parizek, B. R., Anandakrishnan, S., and Alley, R. B.: A viscoelastic flowline model applied to tidal forcing of Bindschadler Ice Stream, West Antarctica, Earth and Planetary Science Letters, 319, 128–132, 2012.

Warburton, K., Hewitt, D., and Neufeld, J.: Shear dilation of subglacial till results in time-dependent sliding laws, Proceedings of the Royal
840   Society A, 479, 20220 536, 2023.

Weertman, J.: On the sliding of glaciers, Journal of glaciology, 3, 33–38, 1957.

Weertman, J.: General theory of water flow at the base of a glacier or ice sheet, Reviews of Geophysics, 10, 287–333, 1972.

Welch, P.: The use of fast Fourier transform for the estimation of power spectra: a method based on time averaging over short, modified periodograms, IEEE Transactions on audio and electroacoustics, 15, 70–73, 1967.

845   Werder, M. A., Hewitt, I. J., Schoof, C. G., and Flowers, G. E.: Modeling channelized and distributed subglacial drainage in two dimensions, Journal of Geophysical Research: Earth Surface, 118, 2140–2158, 2013.

Westermann, S., Ingeman-Nielsen, T., Scheer, J., Aalstad, K., Aga, J., Chaudhary, N., Etzelmüller, B., Filhol, S., Kääb, A., Renette, C., et al.: The CryoGrid community model (version 1.0)–a multi-physics toolbox for climate-driven simulations in the terrestrial cryosphere, Geoscientific Model Development, 16, 2607–2647, 2023.

850   Wiens, D. A., Anandakrishnan, S., Winberry, J. P., and King, M. A.: Simultaneous teleseismic and geodetic observations of the stick–slip motion of an Antarctic ice stream, Nature, 453, 770–774, 2008.

Woodward, J., Murray, T., and McCaig, A.: Formation and reorientation of structure in the surge-type glacier Kongsvegen, Svalbard, Journal of Quaternary Science: Published for the Quaternary Research Association, 17, 201–209, 2002.

Yang, X., Nielsen, K. P., Amstrup, B., Peralta, C., Høyer, J., Englyst, P. N., Schyberg, H., Homleid, M., Kpltzow, M. ø., Randriamampianina,
855   R., Dahlgren, P., Stpylen, E., Valkonen, T., Palmason, B., Thorsteinsson, S., Bojarova, J., Körnich, H., Lindskog, M., Box, J., and Mankoff, K.: C3S Arctic regional reanalysis – Full system documentation, Tech. rep., 2021.

Zhan, Z.: Seismic noise interferometry reveals transverse drainage configuration beneath the surging Bering Glacier, Geophysical Research Letters, 46, 4747–4756, 2019.

Zoet, L. K. and Iverson, N. R.: A slip law for glaciers on deformable beds, Science, 368, 76–78, 2020.

 Appendix A: Full time serie
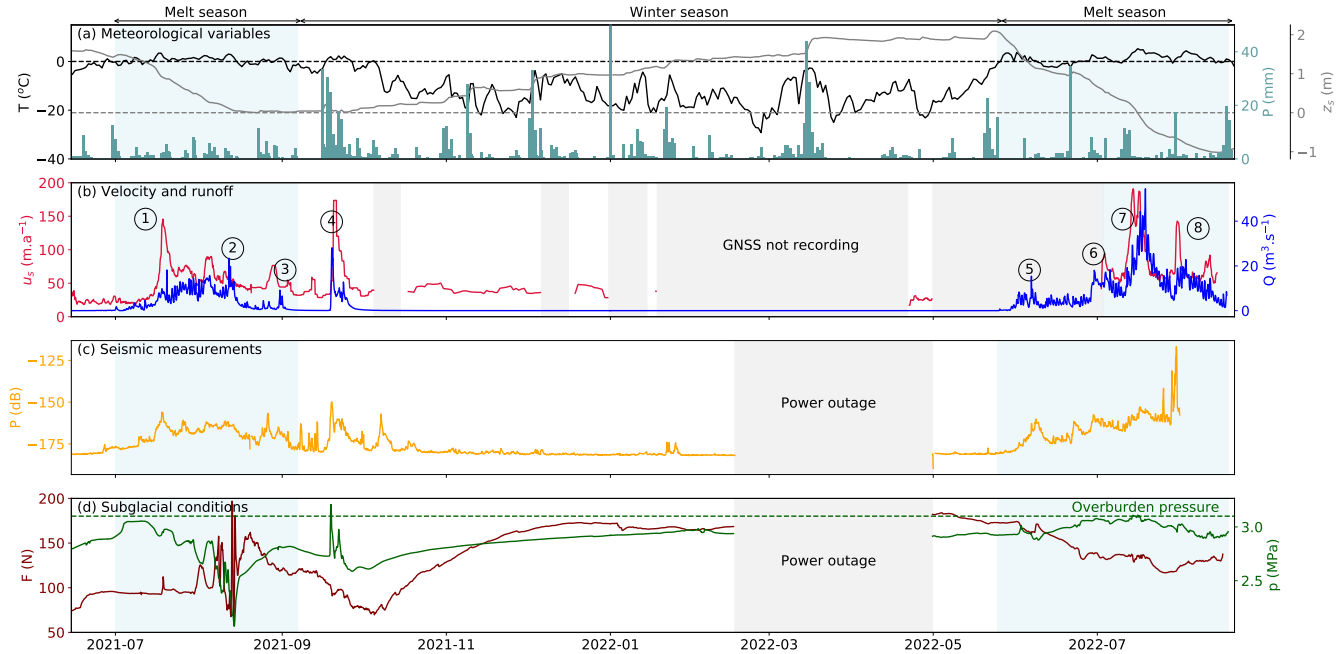
Figure A1. Time series of physical quantities measured from spring 2021 to summer 2022. (a) Temperature (black line), precipitation (light blue bars) from CARRA/AROME-Artic, and relative glacier surface height (grey line) from Cryogrid simulations (Schmidt et al., 2023). The three variables are extracted for the closest grid point of the borehole. In 2022, the surface height is negative which corresponds to ice melt. (b) Modelled runoff (blue line) and glacier surface velocity measured (red line). Circled numbers refer to different episodes described in the main text. (c) turbulent-water-flow-induced seismic power recorded at the surface of the glacier in the 3-10 Hz frequency band (yellow line). (d) Borehole water pressure (green line) and force acting on the ploughmeter (dark red line). Blue shaded areas represent the melt seasons. Grey shaded areas represent periods of missing data.

Appendix B: Pre-processing of the time series

[Need some text here]

Appendix C: Surface velocity data

The velocity record presented in this study combines two different GNSS records. One of the GNSS stations is positioned at

 stake 6 (KNG-6: 13.15153^{o}E 78.78067^{o}N) and the other one at stake 7 (KNG-7: 13.23962^{o}E 78.76770^{o}N). In figure C1, we present the two datasets that have been combined. We apply a one-week moving median for KNG7 velocity to smooth the record especially during the winter period when the velocities are low and thus the daily velocity derivation is less accurate.
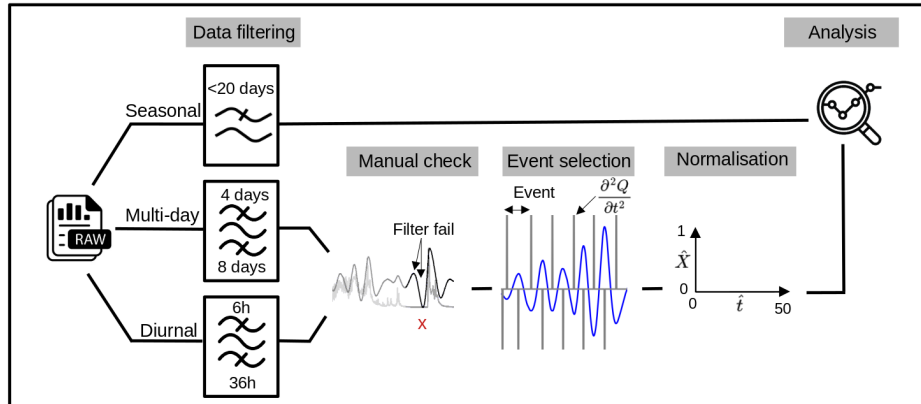
Figure B1. Pre-processing workflow applied to the time series. The original time-series (see Fig. 3 below) have been filtered at three time-scales. The multi-day and diurnal filtered data have been inspected against the unfiltered data to remove spurious artefacts that can be created by the filtering technique (see also Appendix G, G1). We then segmented the recorded data into multiple events and normalised the magnitude and duration of each.
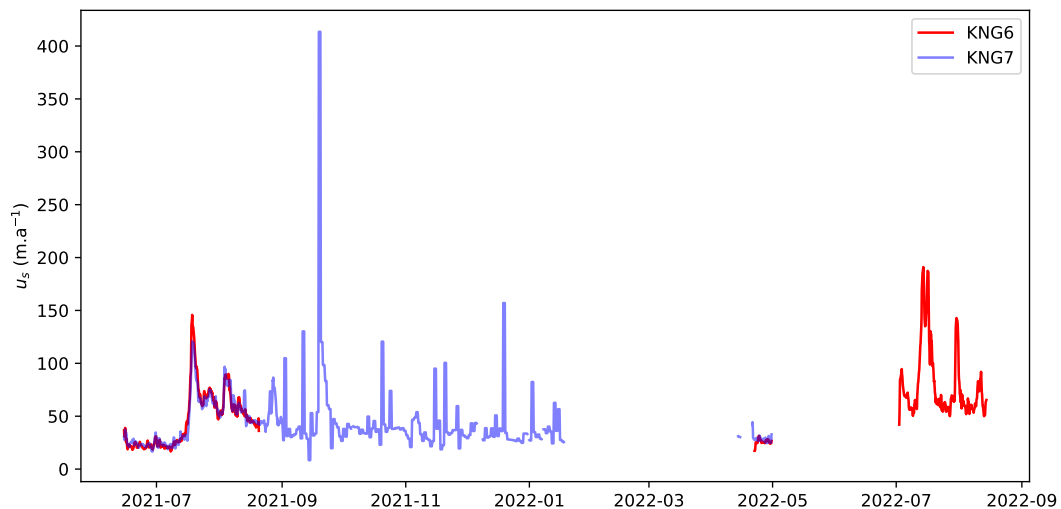
Figure C1. Velocity data series from GNSS stations KNG6 (red curve) and KNG7 (blue curve).

Appendix D: Events

Table D1. Description of the twelve multi-day time scale events during the melt season 2021

Event	Start	Stop	Duration
0	2021-07-01 00:00:00	2021-07-03 03:00:00	2 days 03:00:00
1	2021-07-03 03:00:00	2021-07-13 06:00:00	10 days 03:00:00
2	2021-07-13 06:00:00	2021-07-22 03:00:00	8 days 21:00:00
3	2021-07-22 03:00:00	2021-07-31 03:00:00	9 days 00:00:00
4	2021-07-31 03:00:00	2021-08-08 12:00:00	8 days 09:00:00
5	2021-08-08 12:00:00	2021-08-17 21:00:00	9 days 09:00:00
6	2021-08-17 21:00:00	2021-08-28 00:00:00	10 days 03:00:00
7	2021-08-28 00:00:00	2021-09-04 15:00:00	7 days 15:00:00
8	2021-09-04 15:00:00	2021-09-15 21:00:00	11 days 06:00:00
9	2021-09-15 21:00:00	2021-09-27 03:00:00	11 days 06:00:00
10	2021-09-27 03:00:00	2021-10-04 12:00:00	7 days 09:00:00
11	2021-10-04 12:00:00	2021-10-04 21:00:00	0 days 09:00:00

Table D2. Description of the eight multi-day time scale events during the melt season 2022

Event	Start	Stop	Duration
0	2022-05-25 00:00:00	2022-05-28 21:00:00	3 days 21:00:00
1	2022-05-28 21:00:00	2022-06-10 12:00:00	12 days 15:00:00
2	2022-06-10 12:00:00	2022-06-26 06:00:00	15 days 18:00:00
3	2022-06-26 06:00:00	2022-07-11 06:00:00	15 days 00:00:00
4	2022-07-11 06:00:00	2022-07-23 18:00:00	12 days 12:00:00
5	2022-07-23 18:00:00	2022-08-07 18:00:00	15 days 00:00:00
6	2022-08-07 18:00:00	2022-08-16 00:00:00	8 days 06:00:00
7	2022-08-16 00:00:00	2022-08-16 15:00:00	0 days 15:00:00

Table D3. Description of the 96 diurnal time scale events during the melt season 2021

Event	Start	Stop	Duration	Event	Start	Stop	Duration
0	2021-07-01 00:00:00	2021-07-02 09:00:00	1 days 09:00:00	36	2021-08-06 12:00:00	2021-08-07 03:00:00	0 days 15:00:00
1	2021-07-02 09:00:00	2021-07-03 18:00:00	1 days 09:00:00	37	2021-08-07 03:00:00	2021-08-07 15:00:00	0 days 12:00:00
2	2021-07-03 18:00:00	2021-07-04 15:00:00	0 days 21:00:00	38	2021-08-07 15:00:00	2021-08-08 15:00:00	1 days 00:00:00
3	2021-07-04 15:00:00	2021-07-05 15:00:00	1 days 00:00:00	39	2021-08-08 15:00:00	2021-08-09 15:00:00	1 days 00:00:00
4	2021-07-05 15:00:00	2021-07-06 15:00:00	1 days 00:00:00	40	2021-08-09 15:00:00	2021-08-10 15:00:00	1 days 00:00:00
5	2021-07-06 15:00:00	2021-07-07 15:00:00	1 days 00:00:00	41	2021-08-10 15:00:00	2021-08-11 15:00:00	1 days 00:00:00
6	2021-07-07 15:00:00	2021-07-08 18:00:00	1 days 03:00:00	42	2021-08-11 15:00:00	2021-08-12 15:00:00	1 days 00:00:00
7	2021-07-08 18:00:00	2021-07-09 09:00:00	0 days 15:00:00	43	2021-08-12 15:00:00	2021-08-13 12:00:00	0 days 21:00:00
8	2021-07-09 09:00:00	2021-07-10 15:00:00	1 days 06:00:00	44	2021-08-13 12:00:00	2021-08-14 12:00:00	1 days 00:00:00
9	2021-07-10 15:00:00	2021-07-11 12:00:00	0 days 21:00:00	45	2021-08-14 12:00:00	2021-08-15 15:00:00	1 days 03:00:00
10	2021-07-11 12:00:00	2021-07-12 12:00:00	1 days 00:00:00	46	2021-08-15 15:00:00	2021-08-16 06:00:00	0 days 15:00:00
11	2021-07-12 12:00:00	2021-07-13 18:00:00	1 days 06:00:00	47	2021-08-16 06:00:00	2021-08-16 18:00:00	0 days 12:00:00
12	2021-07-13 18:00:00	2021-07-14 15:00:00	0 days 21:00:00	48	2021-08-16 18:00:00	2021-08-17 18:00:00	1 days 00:00:00
13	2021-07-14 15:00:00	2021-07-15 15:00:00	1 days 00:00:00	49	2021-08-17 18:00:00	2021-08-18 15:00:00	0 days 21:00:00
14	2021-07-15 15:00:00	2021-07-16 12:00:00	0 days 21:00:00	50	2021-08-18 15:00:00	2021-08-19 15:00:00	1 days 00:00:00
15	2021-07-16 12:00:00	2021-07-17 15:00:00	1 days 03:00:00	51	2021-08-19 15:00:00	2021-08-20 18:00:00	1 days 03:00:00
16	2021-07-17 15:00:00	2021-07-18 15:00:00	1 days 00:00:00	52	2021-08-20 18:00:00	2021-08-21 18:00:00	1 days 00:00:00
17	2021-07-18 15:00:00	2021-07-19 15:00:00	1 days 00:00:00	53	2021-08-21 18:00:00	2021-08-22 15:00:00	0 days 21:00:00
18	2021-07-19 15:00:00	2021-07-20 12:00:00	0 days 21:00:00	54	2021-08-22 15:00:00	2021-08-24 12:00:00	1 days 21:00:00
19	2021-07-20 12:00:00	2021-07-21 12:00:00	1 days 00:00:00	55	2021-08-24 12:00:00	2021-08-25 15:00:00	1 days 03:00:00
20	2021-07-21 12:00:00	2021-07-22 15:00:00	1 days 03:00:00	56	2021-08-25 15:00:00	2021-08-26 09:00:00	0 days 18:00:00
21	2021-07-22 15:00:00	2021-07-23 12:00:00	0 days 21:00:00	57	2021-08-26 09:00:00	2021-08-27 15:00:00	1 days 06:00:00
22	2021-07-23 12:00:00	2021-07-24 12:00:00	1 days 00:00:00	58	2021-08-27 15:00:00	2021-08-28 15:00:00	1 days 00:00:00
23	2021-07-24 12:00:00	2021-07-25 12:00:00	1 days 00:00:00	59	2021-08-28 15:00:00	2021-08-29 15:00:00	1 days 00:00:00
24	2021-07-25 12:00:00	2021-07-26 12:00:00	1 days 00:00:00	60	2021-08-29 15:00:00	2021-08-30 12:00:00	0 days 21:00:00
25	2021-07-26 12:00:00	2021-07-27 15:00:00	1 days 03:00:00	61	2021-08-30 12:00:00	2021-08-31 12:00:00	1 days 00:00:00
26	2021-07-27 15:00:00	2021-07-28 15:00:00	1 days 00:00:00	62	2021-08-31 12:00:00	2021-09-01 09:00:00	0 days 21:00:00
27	2021-07-28 15:00:00	2021-07-29 12:00:00	0 days 21:00:00	63	2021-09-01 09:00:00	2021-09-02 06:00:00	0 days 21:00:00
28	2021-07-29 12:00:00	2021-07-30 12:00:00	1 days 00:00:00	64	2021-09-02 06:00:00	2021-09-04 09:00:00	2 days 03:00:00
29	2021-07-30 12:00:00	2021-07-31 15:00:00	1 days 03:00:00	65	2021-09-04 09:00:00	2021-09-05 03:00:00	0 days 18:00:00
30	2021-07-31 15:00:00	2021-08-01 12:00:00	0 days 21:00:00	66	2021-09-05 03:00:00	2021-09-06 00:00:00	0 days 21:00:00
31	2021-08-01 12:00:00	2021-08-02 12:00:00	1 days 00:00:00	67	2021-09-06 00:00:00	2021-09-06 15:00:00	0 days 15:00:00
32	2021-08-02 12:00:00	2021-08-03 06:00:00	0 days 18:00:00	68	2021-09-06 15:00:00	2021-09-07 03:00:00	0 days 12:00:00
33	2021-08-03 06:00:00	2021-08-04 12:00:00	1 days 06:00:00	69	2021-09-07 03:00:00	2021-09-08 00:00:00	0 days 21:00:00
34	2021-08-04 12:00:00	2021-08-05 12:00:00	1 days 00:00:00	70	2021-09-08 00:00:00	2021-09-08 18:00:00	0 days 18:00:00
35	2021-08-05 12:00:00	2021-08-06 12:00:00	1 days 00:00:00	71	2021-09-08 18:00:00	2021-09-09 18:00:00	1 days 00:00:00

Table D3. (Following) Description of the 96 diurnal time scale events during the melt season 2021

Event	Start	Stop	Duration
72	2021-09-09 18:00:00	2021-09-10 18:00:00	1 days 00:00:00
73	2021-09-10 18:00:00	2021-09-11 09:00:00	0 days 15:00:00
74	2021-09-11 09:00:00	2021-09-12 06:00:00	0 days 21:00:00
75	2021-09-12 06:00:00	2021-09-13 03:00:00	0 days 21:00:00
76	2021-09-13 03:00:00	2021-09-14 09:00:00	1 days 06:00:00
77	2021-09-14 09:00:00	2021-09-15 06:00:00	0 days 21:00:00
78	2021-09-15 06:00:00	2021-09-19 00:00:00	3 days 18:00:00
79	2021-09-19 00:00:00	2021-09-20 12:00:00	1 days 12:00:00
80	2021-09-20 12:00:00	2021-09-22 15:00:00	2 days 03:00:00
81	2021-09-22 15:00:00	2021-09-23 06:00:00	0 days 15:00:00
82	2021-09-23 06:00:00	2021-09-24 09:00:00	1 days 03:00:00
83	2021-09-24 09:00:00	2021-09-25 18:00:00	1 days 09:00:00
84	2021-09-25 18:00:00	2021-09-27 00:00:00	1 days 06:00:00
85	2021-09-27 00:00:00	2021-09-27 12:00:00	0 days 12:00:00
86	2021-09-27 12:00:00	2021-09-28 03:00:00	0 days 15:00:00
87	2021-09-28 03:00:00	2021-09-29 03:00:00	1 days 00:00:00
88	2021-09-29 03:00:00	2021-09-29 18:00:00	0 days 15:00:00
89	2021-09-29 18:00:00	2021-09-30 09:00:00	0 days 15:00:00
90	2021-09-30 09:00:00	2021-10-01 03:00:00	0 days 18:00:00
91	2021-10-01 03:00:00	2021-10-02 18:00:00	1 days 15:00:00
92	2021-10-02 18:00:00	2021-10-03 12:00:00	0 days 18:00:00
93	2021-10-03 12:00:00	2021-10-04 00:00:00	0 days 12:00:00
94	2021-10-04 00:00:00	2021-10-04 15:00:00	0 days 15:00:00
95	2021-10-04 15:00:00	2021-10-04 21:00:00	0 days 06:00:00

Table D4. Description of the 85 diurnal time scale events during the melt season 2022

Event	Start	Stop	Duration	Event	Start	Stop	Duration
0	2022-05-25 00:00:00	2022-05-25 06:00:00	0 days 06:00:00	36	2022-06-29 12:00:00	2022-06-30 12:00:00	1 days 00:00:00
1	2022-05-25 06:00:00	2022-05-26 12:00:00	1 days 06:00:00	37	2022-06-30 12:00:00	2022-07-01 12:00:00	1 days 00:00:00
2	2022-05-26 12:00:00	2022-05-27 03:00:00	0 days 15:00:00	38	2022-07-01 12:00:00	2022-07-02 06:00:00	0 days 18:00:00
3	2022-05-27 03:00:00	2022-05-27 18:00:00	0 days 15:00:00	39	2022-07-02 06:00:00	2022-07-03 12:00:00	1 days 06:00:00
4	2022-05-27 18:00:00	2022-05-28 15:00:00	0 days 21:00:00	40	2022-07-03 12:00:00	2022-07-04 12:00:00	1 days 00:00:00
5	2022-05-28 15:00:00	2022-05-29 15:00:00	1 days 00:00:00	41	2022-07-04 12:00:00	2022-07-05 09:00:00	0 days 21:00:00
6	2022-05-29 15:00:00	2022-05-30 15:00:00	1 days 00:00:00	42	2022-07-05 09:00:00	2022-07-06 09:00:00	1 days 00:00:00
7	2022-05-30 15:00:00	2022-05-31 15:00:00	1 days 00:00:00	43	2022-07-06 09:00:00	2022-07-07 09:00:00	1 days 00:00:00
8	2022-05-31 15:00:00	2022-06-01 12:00:00	0 days 21:00:00	44	2022-07-07 09:00:00	2022-07-08 09:00:00	1 days 00:00:00
9	2022-06-01 12:00:00	2022-06-02 15:00:00	1 days 03:00:00	45	2022-07-08 09:00:00	2022-07-09 09:00:00	1 days 00:00:00
10	2022-06-02 15:00:00	2022-06-03 12:00:00	0 days 21:00:00	46	2022-07-09 09:00:00	2022-07-10 12:00:00	1 days 03:00:00
11	2022-06-03 12:00:00	2022-06-04 09:00:00	0 days 21:00:00	47	2022-07-10 12:00:00	2022-07-11 09:00:00	0 days 21:00:00
12	2022-06-04 09:00:00	2022-06-05 15:00:00	1 days 06:00:00	48	2022-07-11 09:00:00	2022-07-12 06:00:00	0 days 21:00:00
13	2022-06-05 15:00:00	2022-06-06 18:00:00	1 days 03:00:00	49	2022-07-12 06:00:00	2022-07-13 06:00:00	1 days 00:00:00
14	2022-06-06 18:00:00	2022-06-07 12:00:00	0 days 18:00:00	50	2022-07-13 06:00:00	2022-07-14 12:00:00	1 days 06:00:00
15	2022-06-07 12:00:00	2022-06-08 15:00:00	1 days 03:00:00	51	2022-07-14 12:00:00	2022-07-15 09:00:00	0 days 21:00:00
16	2022-06-08 15:00:00	2022-06-09 18:00:00	1 days 03:00:00	52	2022-07-15 09:00:00	2022-07-16 09:00:00	1 days 00:00:00
17	2022-06-09 18:00:00	2022-06-10 18:00:00	1 days 00:00:00	53	2022-07-16 09:00:00	2022-07-17 09:00:00	1 days 00:00:00
18	2022-06-10 18:00:00	2022-06-11 15:00:00	0 days 21:00:00	54	2022-07-17 09:00:00	2022-07-18 09:00:00	1 days 00:00:00
19	2022-06-11 15:00:00	2022-06-12 15:00:00	1 days 00:00:00	55	2022-07-18 09:00:00	2022-07-19 09:00:00	1 days 00:00:00
20	2022-06-12 15:00:00	2022-06-13 15:00:00	1 days 00:00:00	56	2022-07-19 09:00:00	2022-07-20 09:00:00	1 days 00:00:00
21	2022-06-13 15:00:00	2022-06-14 15:00:00	1 days 00:00:00	57	2022-07-20 09:00:00	2022-07-21 09:00:00	1 days 00:00:00
22	2022-06-14 15:00:00	2022-06-15 15:00:00	1 days 00:00:00	58	2022-07-21 09:00:00	2022-07-22 09:00:00	1 days 00:00:00
23	2022-06-15 15:00:00	2022-06-16 15:00:00	1 days 00:00:00	59	2022-07-22 09:00:00	2022-07-23 06:00:00	0 days 21:00:00
24	2022-06-16 15:00:00	2022-06-17 18:00:00	1 days 03:00:00	60	2022-07-23 06:00:00	2022-07-24 09:00:00	1 days 03:00:00
25	2022-06-17 18:00:00	2022-06-18 12:00:00	0 days 18:00:00	61	2022-07-24 09:00:00	2022-07-25 06:00:00	0 days 21:00:00
26	2022-06-18 12:00:00	2022-06-19 15:00:00	1 days 03:00:00	62	2022-07-25 06:00:00	2022-07-26 09:00:00	1 days 03:00:00
27	2022-06-19 15:00:00	2022-06-21 15:00:00	2 days 00:00:00	63	2022-07-26 09:00:00	2022-07-27 09:00:00	1 days 00:00:00
28	2022-06-21 15:00:00	2022-06-22 12:00:00	0 days 21:00:00	64	2022-07-27 09:00:00	2022-07-28 09:00:00	1 days 00:00:00
29	2022-06-22 12:00:00	2022-06-23 09:00:00	0 days 21:00:00	65	2022-07-28 09:00:00	2022-07-29 09:00:00	1 days 00:00:00
30	2022-06-23 09:00:00	2022-06-24 12:00:00	1 days 03:00:00	66	2022-07-29 09:00:00	2022-07-30 06:00:00	0 days 21:00:00
31	2022-06-24 12:00:00	2022-06-25 12:00:00	1 days 00:00:00	67	2022-07-30 06:00:00	2022-07-31 09:00:00	1 days 03:00:00
32	2022-06-25 12:00:00	2022-06-26 12:00:00	1 days 00:00:00	68	2022-07-31 09:00:00	2022-08-01 06:00:00	0 days 21:00:00
33	2022-06-26 12:00:00	2022-06-27 15:00:00	1 days 03:00:00	69	2022-08-01 06:00:00	2022-08-02 09:00:00	1 days 03:00:00
34	2022-06-27 15:00:00	2022-06-28 09:00:00	0 days 18:00:00	70	2022-08-02 09:00:00	2022-08-03 09:00:00	1 days 00:00:00
35	2022-06-28 09:00:00	2022-06-29 12:00:00	1 days 03:00:00	71	2022-08-03 09:00:00	2022-08-04 06:00:00	0 days 21:00:00

Table D4. (Following) Description of the 85 diurnal time scale events during the melt season 2022

Event	Start	Stop	Duration
72	2022-08-04 06:00:00	2022-08-05 09:00:00	1 days 03:00:00
73	2022-08-05 09:00:00	2022-08-06 09:00:00	1 days 00:00:00
74	2022-08-06 09:00:00	2022-08-07 09:00:00	1 days 00:00:00
75	2022-08-07 09:00:00	2022-08-08 09:00:00	1 days 00:00:00
76	2022-08-08 09:00:00	2022-08-09 09:00:00	1 days 00:00:00
77	2022-08-09 09:00:00	2022-08-10 09:00:00	1 days 00:00:00
78	2022-08-10 09:00:00	2022-08-11 09:00:00	1 days 00:00:00
79	2022-08-11 09:00:00	2022-08-12 09:00:00	1 days 00:00:00
80	2022-08-12 09:00:00	2022-08-13 09:00:00	1 days 00:00:00
81	2022-08-13 09:00:00	2022-08-14 09:00:00	1 days 00:00:00
82	2022-08-14 09:00:00	2022-08-15 12:00:00	1 days 03:00:00
83	2022-08-15 12:00:00	2022-08-16 09:00:00	0 days 21:00:00
84	2022-08-16 09:00:00	2022-08-16 15:00:00	0 days 06:00:00

Appendix E: Spectrogram

870   Large seasonal changes in turbulent-water-flow-induced seismic power, P are observed within the 3–10 Hz frequency range, in which P is higher by more than two orders of magnitude during the melt season (mid-May to September) compared to winter (Fig. E1). Changes in P are also observed within the 10–20 Hz frequency range, with P during the melt season being about an order of magnitude larger than in winter (Fig. E1).
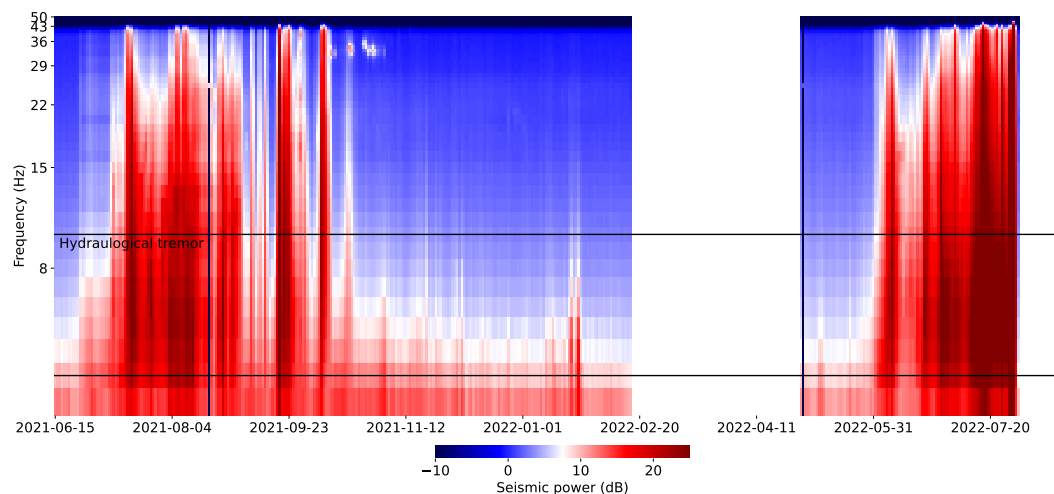
Figure E1. Spectrogram of the observed seismic power P as a function of time on the x-axis and frequency on the y-axis. Colours represent seismic power on a decimal logarithmic scale. White bands are data gaps. The two black lines delineate the frequency band between 3 and 10 Hz that we used in this study.

Appendix F: Metrics used in the classification

875   Figure F1 provides a visual representation of the metrics used to classify the events.
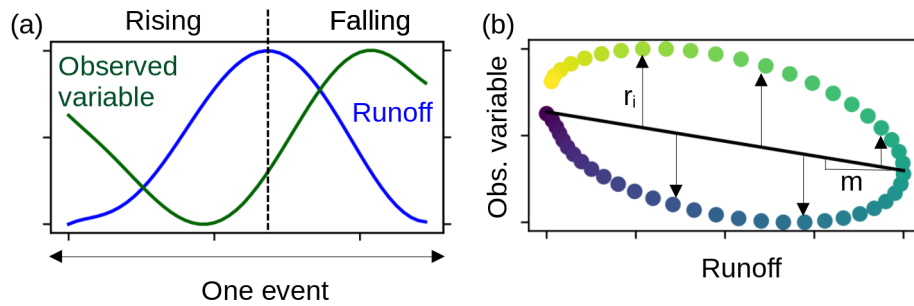
Figure F1. Description of the metrics used to classify the events. (a) Description of one event with the rising and falling part of the runoff to calculate the hysteresis θ. (b) The linear fit used to calculate the residual sum of squares RSS and its slope, m.

Appendix G: Band pass-filtered time series

We have filtered the original time series to determine the different frequency signatures separately. For the seasonal scale, we have applied a low-pass filter with a cutoff at 20 days (Fig. G1 a). For the multi-day scale, we have applied a band-pass filter between four and eight days (Fig. G1 b). For the daily time-scale, we have applied a band-pass filter between six hours and 36 hours (Fig. G1 b).
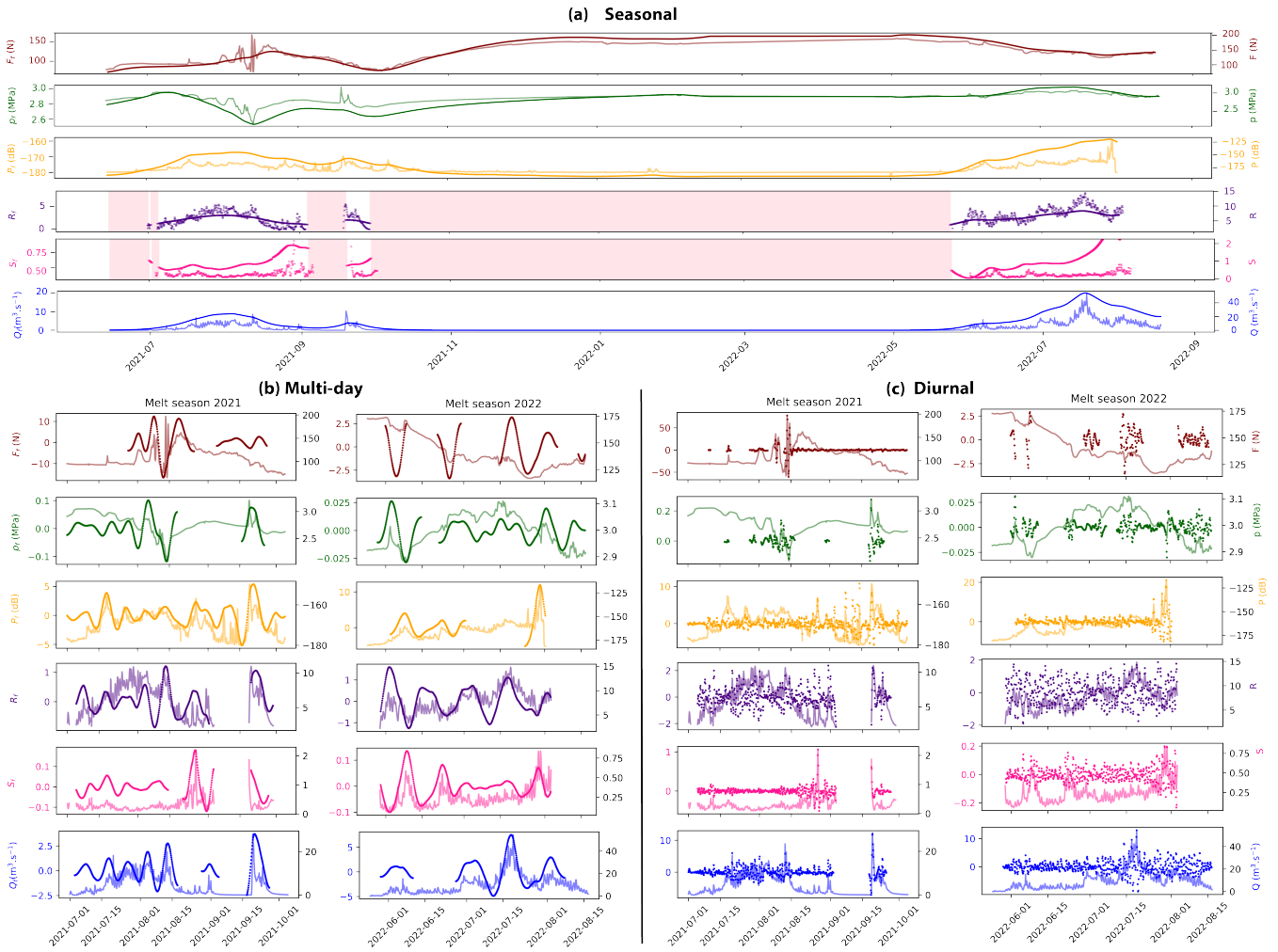
Figure G1. Band-pass filtered series for (a) seasonal (>20 days), multi-day (four to eight days) and diurnal (6h to 36h) time scales. For the last two series, we have computed the band-pass time series for the melt season time period only.

Appendix H: Frequency content of the time series between 6h and 10 days

Figure H1 shows the frequency content of all variables over the recording period between a period of 6h and a period of 10 days. While the force and the water pressure have only episodic frequency content on the scale of one day, the other variables exhibit longer periods with variations on that time scale, but still concentrated during the melting season.
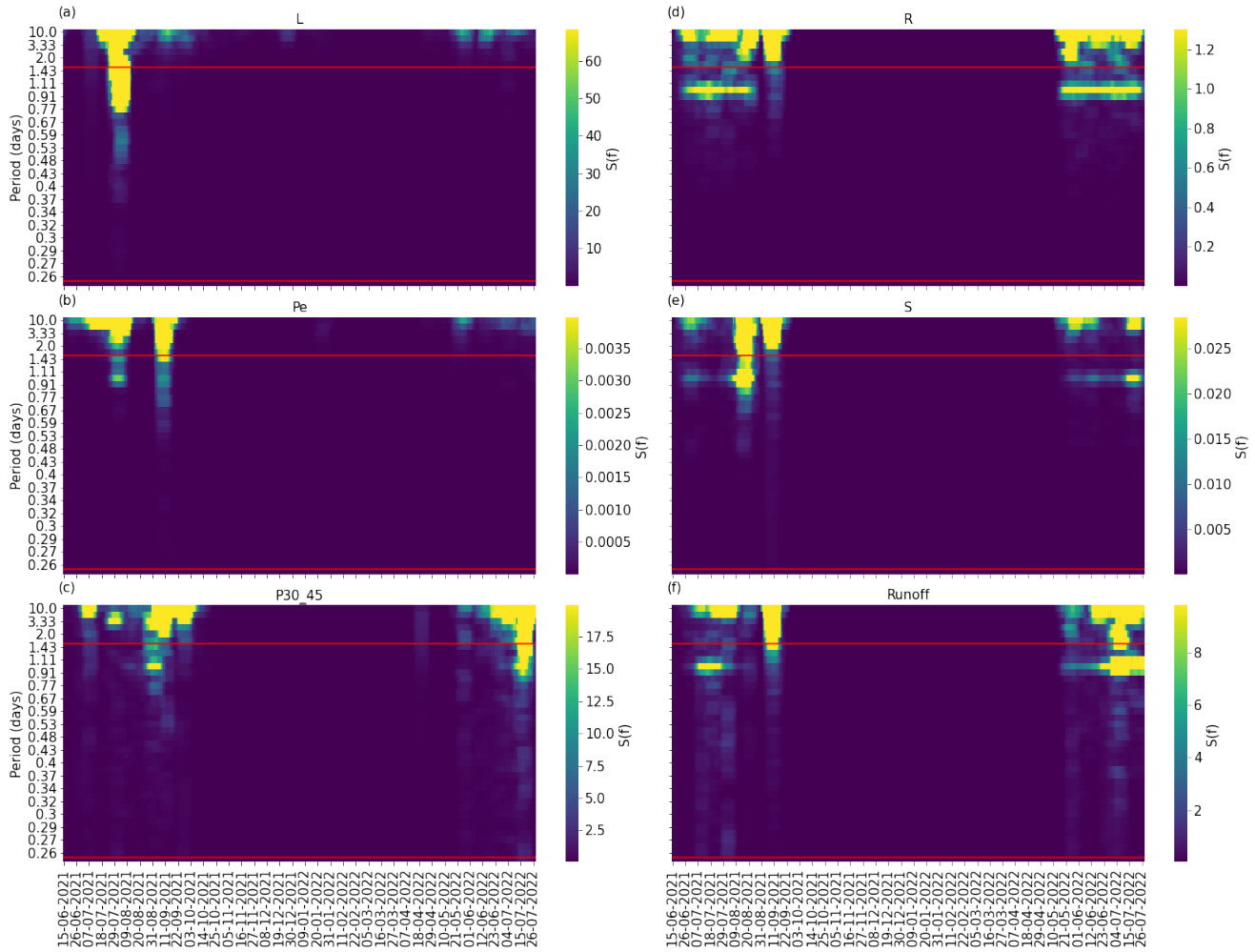
Figure H1. Frequency content intensity for all the variables between 6h an 10 days over the year. The red lines delineate the diurnal frequency content (between 6h and 36h).